Design and Modeling of a Soil-Based Energy Harvester for Underground Wireless Sensor Nodes

by

Md Rubayatur Bhuyian

A thesis
presented to the University of Waterloo
in fulfillment of the
thesis requirement for the degree of
Master of Applied Science
in
Electrical and Computer Engineering

Waterloo, Ontario, Canada, 2020

I hereby declare that I am the sole author of this thesis. This is a true copy of the thesis, including any required final revisions, as accepted by my examiners.

I understand that my thesis may be made electronically available to the public.

Abstract

Wireless Sensor Networks (WSN) have emerged as a reliable and viable solution for monitoring complex large-scale strategic assets that are placed in harsh and hostile environments. Some of the major application areas include environmental monitoring, disaster management, infrastructure monitoring, and security. A large number of such infrastructures are buried underground and have a limited service life. It is important to assess their condition throughout their life cycle to avoid possible catastrophic failures due to their deterioration. Monitoring such infrastructures creates a complex wireless sensor network with thousands of sensor nodes that are required to be functional with zero maintenance for 10∼20 years once deployed. Powering such Wireless Sensors (WS) for decades is a key challenge in the design and operation of WSN.

Sacrificial Anode Cathodic Protection (SACP) technique is a well-known technique for corrosion protection. In this technique, steel structures are protected from natural corrosion by enabling an externally connected anode material to deplete over time. To model the depletion rate of the anode for replacement purposes, human readers visit each Sacrificial Anode (SA) site to take voltage and current measurements once a month. This approach is expensive and prone to human errors. Moreover, there is a large number of such sites in a city. The main challenge in using WSN in such scenarios is providing a reliable source of energy to power the sensor nodes. As the majority part of the structure is buried underground, traditional renewable energy sources, such as solar, wind, and thermal do not offer any lucrative solution due to their requirements for additional setup, space, and periodic maintenance.

Thus, an underground soil-based energy harvester using the existing setup has been carefully researched, designed, developed and implemented as part of this research. The technique exploits the electric current flowing from the cathode to the anode to energize the sensor nodes. The prototype developed in the lab uses the harvested energy from soil to power sensor nodes to communicate the data to the cloud. To develop and implement the prototype two test benches were set up, one indoor and the other outdoor. The outdoor setup facilitated the experiments under varying weather conditions and with the indoor one, experiments were conducted under a controlled environment.

The prototype developed in the lab will be buried underground for security purposes, as a result, data needs to be transmitted through the soil between nodes. Radio Frequency (RF) transmission through the soil is one of the main challenges for this project. Various parameters affect RF signal attenuation in soil (i.e. transmission frequency, burial depth, soil dielectric properties, etc.). In this research, we have investigated, tested and

implemented several wireless technology modules such as Global System for Mobile Communications (GSM), Wireless Fidelity (Wi-Fi), Zigbee, Narrow Band-Internet of Things (NB-IoT) to meet the desired requirements.

The research also outlines the complete operation of the developed module. In addition to that, to estimate the energy harvesting rate, energy harvesting efficiency and to analyze the charging behavior several experiments were conducted to obtain the Current-Voltage (I-V) and the Power-Voltage (P-V) characteristics of the energy source. This study is later used to develop a model for the energy source. The model is validated with measurement data from the field trials. This developed model is helpful to easily realize a system and can be useful to solve numerical problems, find information about the operating point or to analyze a circuit.

Acknowledgements

In the name of Allah, the Most Gracious and the Most Merciful.

All praises to almighty Allah who guided and blessed me throughout my work and my entire life.

I would like to express my sincere appreciation to my supervisor, Prof. Kshirasagar Naik, for his guidance and constant support. His invaluable help of constructive comments and suggestions throughout the experimental and thesis works have contributed to the success of this research.

I would also like to thank my colleagues, Mustafa Al-tekreeti, Abdurhman Albasir, Imtiaz Ahmed Khan, and Kunal Taneja for their constant support and guidance. I am very blessed to have such nice people around me.

Last but surely not least, I would like to thank my parents for their continuous support, patience, and prayers. Special gratitude to my wife, Mumtahina Rahman Mim, for her love, patience and all the sacrifices. Without her sacrifices, I wouldn't have been able to complete my studies. Finally, I would like to the opportunity to thank my lovely daughter, Ayra, who is my inspiration behind everything.

Dedication

To my family for their endless love, encouragement & support.

Table of Contents

List of Tables

List of Figures

Abbreviations

AP Access Point 23, 24, 26

BTS Base Transceiver Station 27, 28

CP Corrotion Protection 2, 3

DC Direct Current 6, 7, 9, 25, 49, 51

EH Energy Harvesting 9, 10, 17, 31

EH-WSN Energy Harvesting- Wireless Sensor Network 10

GSM Global System for Mobile Communications iv, 26, 30, 36

I-V Current-Voltage iv, 49, 60

ICCP Impressed Current Cathodic Protection 7

MPP Maximum Power Point 50

NB-IoT Narrow Band-Internet of Things iv

P-V Power-Voltage iv, 50, 53, 60

PV Photovoltaic 44

RF Radio Frequency iii

RSSI Received Signal Strength Indicator 20, 25

SA Sacrificial Anode iii, 3

SACP Sacrificial Anode Cathodic Protection iii, 2, 3, 5–7, 10, 30, 44, 63

SOC State of Charge 2

SSID Service Set Identifier 23

TSCH Times Slotted Channel Hopping 17

USB Universal Serial Bus 27

Wi-Fi Wireless Fidelity iv, 23

WS Wireless Sensors iii, 1, 20, 22, 30, 31, 63

WSN Wireless Sensor Networks iii, 1–3, 9, 10, 63

Chapter 1

Introduction

This chapter presents the motivation behind this research in Section 1.1, defines the problem statement in Section 1.2, states the solution strategies & goals of the thesis in Section 1.3, and finally goes through the thesis organization and gives a summary of each chapter in Section 1.4.

1.1 Motivation

We are witnessing much progress in the field of WSN for the purpose of monitoring large scale strategic assets, namely, underground water supply systems in cities, roads and bridges, and natural habitats [30]. Three key characteristics of WSN are: (i) each WSN comprises of thousands of sensors; (ii) each WSN is expected to be functional for 10–20 years; and (iii) once deployed, the sensors should operate unattended for their lifetime.

Powering such wireless sensors for decades is a key challenge in the design and operation of WSN [31, 25]. Essentially, the reliability, lifetime, and usefulness of a large-scale WSN will be determined by its power sources [28]. Some conventional ways of powering a WS are as follows [18]: (i) connect the wireless sensors to standard power grids; (ii) connect a long-lasting battery to the sensor; (iii) design each sensor with a rechargeable battery connected to a solar panel.

While the first solution suffers form scalability problem, the second one severely limits the lifetime of a sensor network to a few months. Although the third solution appears to be promising but requires much space and exposure to the sun, and its reliability is extremely low if the solar panels are not periodically cleaned.

The majority of the steel water pipes (cathodes) connecting homes to the mains are buried underground. It is crucial to protect the steel structures from natural corrosion to avoid potential catastrophic failure. Corrotion Protection (CP) is often used to protect steel from corrosion. A common method for CP is SACP technique [4], where steel structures are protected from natural corrosion by enabling an externally connected anode material to deplete over time. Magnesium is commonly used as the anode. To model the depletion rate of the anode for replacement purposes, human readers need to visit each SA site to take measurements of voltage and current once a month. Such an approach is not only expensive but also prone to human errors; additionally, such systems lack scalability.

Using WSN to report the measurement data can be a solution but this technique requires a reliable power source at each CP site. As there are thousands of CP sites which are placed hundreds of meters away, powering them through conventional power source is impractical. As the majority part of the structure is buried underground, traditional energy harvesting sources, such as solar, wind, and thermal do not offer any lucrative solution due to their requirements for additional setup, space, and periodic maintenance. Hence, any effort to collect the current data from each CP site by means of a WSN will require each sensor to be powered with harvested energy from the operational environment.

1.2 Problem Statement

Monitoring the depletion rate of an anode block is very crucial to avoid any catastrophic failure of underground water pipelines or oil lines. Currently, this is done manually by visiting each site by a human reader which is expensive, error-prone and lacks scalability. Automating the process using WSN can solve the problem but requires a reliable power source at each SA site. Conventional power sources are not available every where and typical renewable energy sources require additional setup and moreover suffer from reliability and maintenance issues.

1.3 Solution Strategy & Contributions

To address the problem mentioned above, the research focuses on powering up the wireless sensors WSN with non-conventional power sources and optimally utilizing the available State of Charge (SOC) of the energy storage unit of each sensor to operate the WSNs in harsh environments with no human intervention after deployment. Specifically, the research concentrates on harvesting energy from the operational environment, i.e soil, to

power up the individual sensors. A prototype of a soil-based energy harvesting WSN has been proposed to facilitate the collection of voltage and current measurements at each SA site. We exploit the electric current flowing from the cathode to the anode to charge a supercapacitor and energize the sensor node. This work demonstrates the design and development of the prototype. Characterization of the energy source has been done through multiple experiments and based on that a model has been developed. It also elaborates on finding different parameters of the developed model. Rate of energy harvesting and also energy requirements of different sensor nodes under different operating conditions have been also addressed. To validate the proposed model, results from field trials were compared with simulation results from MATLAB. The obtained results show the practicality of the proposed solution.

This research makes the following contributions:

- Designs and develops a WSN prototype to monitor the corrosion characteristics of water pipelines protected via the well-known SACP technique.
- Analyzes the power consumption characteristics of typical sensor nodes and identifies various factors that affect the system lifetime and communication reliability.
- Characterizes and models the energy source and finding different parameters of the model.
- Validates the model with measurement data from field trials.

1.4 Thesis Organization

The remainder of the thesis is organized as follows:

Chapter 2 presents a brief background on topics such as CP, different CP techniques and different energy harvesting techniques commonly used. It also discusses related works by other researchers.

Chapter 3 gives a general overview of the proposed system and describes the test bench setup. It gives details on the hardware components and the software components used, as well as the detailed selection criteria of the communication based on experiments and results.

Chapter 4 introduces the design development of the proposed system and explains all the steps in detail. It discusses different stages of the design, talks about the actual implementation of the hardware and different configuration settings.

Chapter 5 outlines the experimental step and tests to be done to characterize model the energy source. It shows the methods to calculate different parameters of the model and presents the equivalent circuit.

Chapter 6 verifies the proposed model by comparing the results obtained from the proposed model with the simulation results from MATLAB. It also talks about the accuracy of the proposed model.

Chapter 7 concludes the thesis.

Chapter 2

Background and Related Works

This chapter provides a general introduction to related topics, briefly discusses important tools and techniques used in the research, and reviews existing work by other researchers on the subject. The presentation here is intended to clarify the research work for readers and not be exhaustive.

2.1 Basic principle of cathodic protection

Cathodic protection limits the corrosion of a metal surface by making it the cathode of an electrochemical cell and is achieved in two ways:

- Sacrificial Anode Cathodic Protection (SACP)
- Impressed Current Cathodic Protection (ICCP)

The former includes the structure as part of a spontaneous galvanic cell, and the latter includes the structure as part of a driven electrochemical cell.

An overview of the SACP technique to protect steel pipes from corrosion has been illustrated in figure 2.1. A steel pipe buried in the ground will be subject to natural corrosion, and the most effective technique to protect it is to bury a block of magnesium near the steel pipe. In an electrical sense, the steel pipe acts as the cathode and the magnesium block acts as the anode, and the two metal blocks are simply connected by means of an electrical conductor, as illustrated in figure 2.1. In the absence of the SACP

mechanism, the steel pipe will externally corrode at its natural rate determined by its environment (namely, chemical composition, availability of oxygen on the steel surface, moisture content of the soil, and temperature). However, with the SACP mechanism in place, it is the anode block that will gradually dissolve in the soil, thereby protecting the cathode block. In other words, corrosion of the steel cathode is minimized at the expense of the magnesium anode. Hence the anode block is called the sacrificial anode, and the technique is known as Sacrificial Anode Cathodic Protection. Over time, the anode will be completely dissolved in soil and it will stop protecting the cathode (i.e. steel pipe). Therefore, modeling and estimating the lifetime of the anode is key to protecting the steel pipes, because new anode blocks can be installed to continue to provide protection.

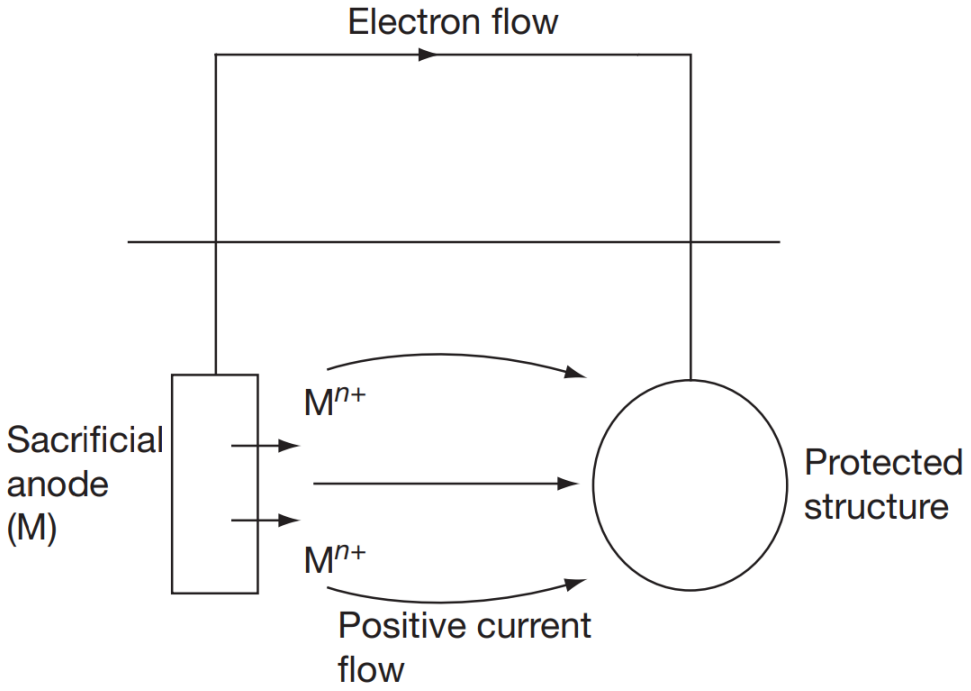

Figure 2.1: Schematic diagram of cathodic protection using sacrificial anodes [4].

In ICCP, inert anodes are used and a Direct Current (DC) is impressed onto the cathode surface with an external DC source. In other words, a DC source is inserted into the connector between the anode and the cathode, so that the impressed current flows onto the cathode.

Steel structures, whether embedded in concrete, soil, or water, are protected by applying

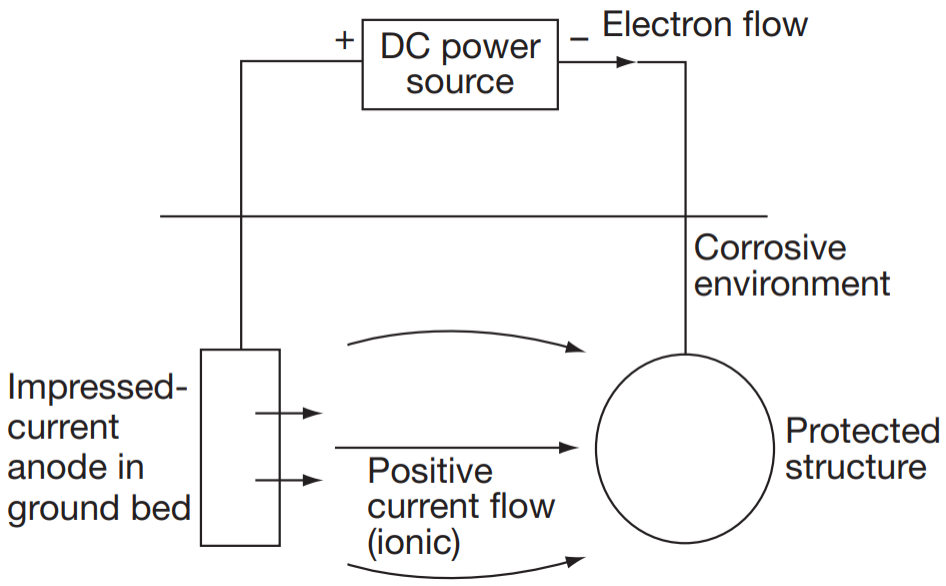

Figure 2.2: Schematic diagram of cathodic protection using the impressed-current technique [4].

the SACP or Impressed Current Cathodic Protection (ICCP) technique [23, 22, 35, 9, 37]. ICCP is preferred where widespread protection is required, namely, in reinforced concrete structures [9], but it needs a constant DC power supply. However, the ICCP technique was not applied to the underground network of water pipelines because of the difficulties in powering a large number of anode blocks located hundreds of meters apart. In other words, there is no reliable power source at the anode blocks. Hence, any effort to collect the current data from each CP site by means of a WSN will require each sensor to be powered with harvested energy.

2.2 Service life Estimation of Anode Blocks

The anode material in an SACP system depletes over time. If the remaining amount of the anode material is not enough to provide protection, then the service life (T_S) of the SACP system is over. Accurate estimation of (T_S) is essential to trigger preventive maintenance tasks to continuously provide the SACP protection. The amount of electrical charges flowing between the protected cathode and the anode is an important measurable

parameter in estimating the service life of an SACP system. It's governed by Faraday's Law [38]:

$$Lm = (Q/Fc) \times (Mm/Vm) \tag{2.1}$$

where Lm is the loss of mass of anode material expressed in grams (g), Q is the amount of charge flowing between anode and cathode expressed in coulombs (C), Fc is the Faraday's constant ($96500C/mol$), Mm is the molecular mass of the anode material, Vm is valency number of the anode material. For example, if Zinc is used as the anode material, then $Mm = 65.382g/mol$ and $Vm = 2$. Considering the fact that Fc, Mm, Vm are constants for a given anode material, we can rewrite Eq. (6.1) as follows:

$$Lm = Cm \times Q \tag{2.2}$$

where, the constant Cm is given by:

$$Cm = (1/Fc) \times (Mm/Vm) \tag{2.3}$$

To introduce time, we rewrite Eq. (6.2) as shown below:

$$Lm(t) = Cm \times Q(t) \tag{2.4}$$

Thus, Eq. (2.4) can be rewritten as:

$$Lm(t) = Cm \times \int_0^t i(t)dt \tag{2.5}$$

where $i(t)$ is the instantaneous current flowing between the anode and the cathode. To estimate the service life, Ts, of a single SACP protection node comprising a cathode (water pipe) and a single anode block, we assume that the anode material depletes at a constant rate and it becomes completely depleted by the end of the service life Ts. A constant rate depletion implies that the current (I) flowing between the anode and the cathode is constant. Therefore, Eq. (2.5) can be rewritten as:

$$Am = Cm \times I \times Ts \tag{2.6}$$

where Am is the Initial mass of an anode block. Therefore, the service life (Ts) is evaluated by:

$$Ts = Am/(Cm \times I) \tag{2.7}$$

However, from a practical standpoint, an anode block stops providing protection service once the remaining mass of an anode block falls by α percent of the original mass Am, where α is a design parameter. In other words, the remaining anode mass $(1–\alpha)Am$ does not contribute to protecting the cathode. Thus, Eq. (2.7) is remodeled as:

$$Ts = \alpha Am/(Cm \times I) \tag{2.8}$$

The challenge in applying Eq. (2.8) to estimate the service life of a cathodic protection node lies in finding the value of I, which is the mean value of the current flowing between the anode and the cathode. The instantaneous value of the current, $i(t)$, is a highly varying quantity that is influenced by the surrounding environment. Therefore, Ts could be estimated by continuously measuring $i(t)$ for an adequate period of time (several months). Initial, long-term monitoring of $i(t)$ would be a key factor in accurately estimating the value of Ts. The estimation model will be validated by actually measuring the loss of anode mass for some strategically placed anodes.

2.3 Energy Harvesting Techniques

Energy Harvesting (EH) covers several methods that use physical phenomena to collect various forms of electrical energy at a micro-level. The four broad EH methods are: (i) solar and light energy harvesting; (ii) mechanical energy harvesting; (iii) thermoelectric energy harvesting; and (iv) electromagnetic energy harvesting. For all WSN applications, there cannot be a single, universal source of EH because different applications have different physical operational environments. A stable power source for a WSN node has four stages: (i) first, energy is collected from the environment by means of an EH technique; (ii) in the second stage, known as a rectifier, power is converted into DC power; (iii) in the third stage, known as a buffer, energy is accumulated in a storage unit comprising batteries, supercapacitors, or fuel cells; and (iv) in the fourth stage, the output power is stabilized to a constant voltage. The third (buffer) stage needs to have high energy density (Joules/cm3 or Joules/gm), whereas the remaining three stages need to be energy efficient. Energy harvesting has become indispensable in monitoring huge swathes of the environment, and some continuously open issues concerning EH are: (i) increasing the size of EH elements to enhance their energy yield efficiency; (ii) combining multiple EH techniques on the same sensor node [40]; and (iii) exploring new EH techniques for specific applications.

2.4 Related work

Recently, many practical deployments of WSNs have been reported in which different EH techniques are used [18, 44, 8]. In one work, an air quality monitoring system was developed where sensor nodes were powered from multiple energy sources, namely, solar, thermoelectric, radiofrequency, and piezoelectric vibration [19]. Supercapacitors were used to store the harvested energy. A WSN of 400 tree-mounted sensor nodes was deployed to monitor wildfire in the Uwharrie forest in California where each sensor node was powered by a micro windmill-structured turbine that delivers 3 mW of power at a wind speed of 3 m/s [42]. For corrosion monitoring, several works have reported the use of solar, thermal gradient, wind, and piezoelectric vibration to power sensor nodes [32, 21, 6]. In another application, corrosion energy was suggested to produce the required energy to power the wireless sensor nodes [45], [33]. However, all the applications were about corrosion monitoring in reinforced concrete structures, and no experimental data were presented. In another work, a methodology was developed to convert water movement in a water distribution system to electrical energy to energize a WSN that monitors underground water pipelines [43]. To the best of our knowledge, no prior work has reported the utilization of the SACP technique to harvest energy for the WSN that monitors the corrosion characteristics in water pipelines.

An Energy Harvesting- Wireless Sensor Network (EH-WSN) node running on harvested energy may not have enough energy available for continuous operation. Therefore, service tasks and the energy harvesting task on a node must be appropriately scheduled [24]. Kosunalp [27] surveyed several MAC protocols for nodes in an EH-WSN to exploit ambient energy. The design of energy-efficient MAC protocols, which have been inspired by receiver-initiated architecture, is important because communication in a WSN is more energy consuming than computation. Those MAC protocols attempt to maximize the lifetime of EH-WSN by balancing energy usage due to data transfer with the rate of energy harvesting. Tan and Yan [34] modeled an energy harvesting embedded system module with a task model, an energy model, and a resource model, and proposed a dynamic task scheduling algorithm. The scheduling algorithm dynamically concentrates the dispersed idle time periods together to harvest energy, thereby enabling the embedded system to have long contiguous periods for energy harvesting and long contiguous periods to execute the service task [1].

Chapter 3

Test Bench Preparation

This section gives an overview of the test bench that has been prepared and used for different experiments & tests. The general structure of the system is outlined here and talks about different hardware that has been used. The criteria for choosing the communication board and detail test setups of underground tests and outcomes are discussed here. Finally, concludes with a selection of a communication board after analyzing the results of the tests.

3.1 General Overview

The general structure of the proposed system is shown in Figure 3.1. The flow of energy, data, and control paths are represented by solid, dotted, and dashed lines, respectively. The EH module collects energy from the movement of electrons between the anode and cathode that are buried into the soil. The EH module mainly comprises an ultra-low voltage step-up DC/DC converter, a storage device, and a switch to control the power flow. The switch ensures that the sensor node is powered only when the output voltage is at the specified level. The WS node is responsible for sensing the current $i(t)$ and transmitting the data to the sink node.

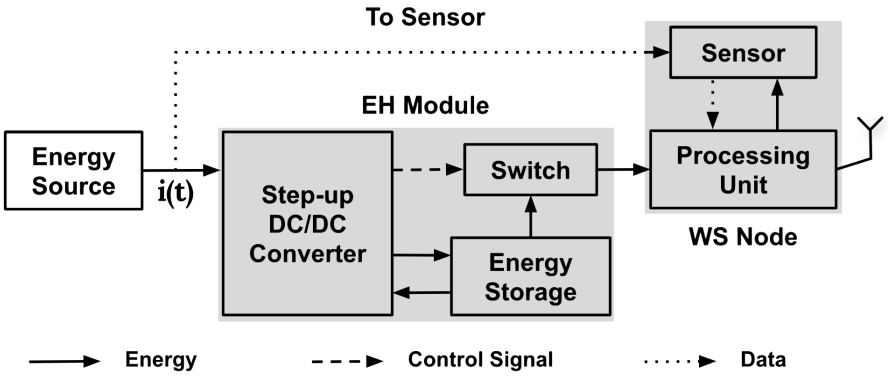

Figure 3.1: General Structure

3.2 Lab setup to replicate an actual SA site

Figure 3.2 shows the lab setup to replicate an actual SA site where a block of Magnesium is buried under the soil along with a galvanized steel pipe that needs to be protected. The steel pipe acts as a cathode and the Magnesium block acts as an anode of an electrochemical cell, and the output is taken simply from the terminals of two metal blocks.

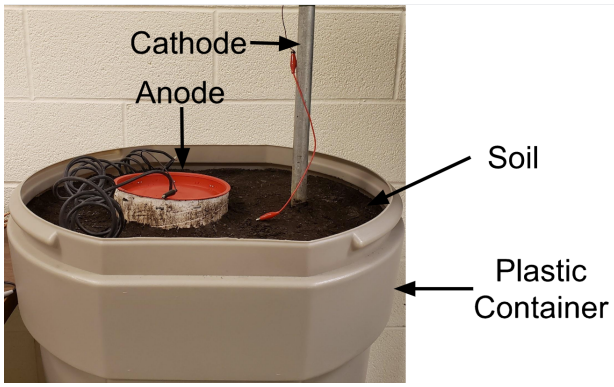

Figure 3.2: Lab setup to replicate an actual SA site.

The anode block used to harvest energy from the soil is depicted in 3.3(a). Only one anode block is required for each setup. The physical dimensions of the anode block are shown in figure 3.3(b)

Figure 3.4(a) shows the container which has been used for this particular application. Anode block along with soil and the galvanized pipe is placed inside the container to

(a) Anode Block

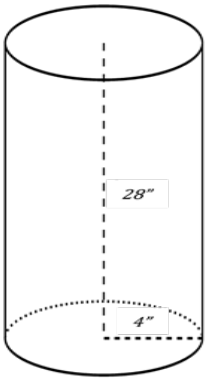

(b) Anode Block Dimension

Figure 3.3: Specification of the Anode Block

harvest energy from the soil. The physical dimensions of the container used are shown in figure 3.4(b).

(a) Rain Barrel

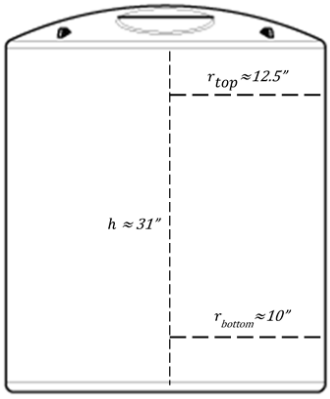

(b) Rain Barrel Dimension

Figure 3.4: Specification of the Container

3.2.1 Test Environments

It is very important to observe the behavior of the energy source under different conditions to get an insight into the energy harvesting rate under different weather conditions. To do so the tests were carried out in two different setups.

- Indoor Setup

  In the Indoor setup, the tests were carried out in controlled conditions where the temperate, humidity and moisture of the soil were kept constant throughout the time.

- Outdoor setup

  In the outdoor setup, the source was exposed to varying weather conditions where the temperate, humidity and moisture of the soil were varying naturally.

(a) Indoor Setup (b) Outdoor Setup

Figure 3.5: Test setups under different environments

3.3 EH Module

The EH module is realized by the demo board DC2042A [12] from Analog Devices. This board consists of four energy harvesting ICs. For our application, we utilize the energy

harvester chip LTC3108 [16]. This chip is an integrated DC/DC converter ideal for harvesting and managing surplus energy from extremely low input voltage sources. The chip can operate from input voltages as low as 20 mV.

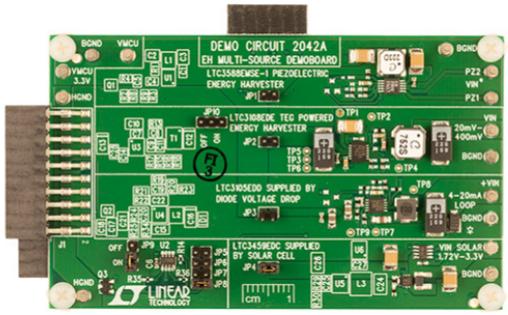

Figure 3.6: DC2042A Development Board [12]

Fifteen optional energy storage capacitors are available on-board to be used by the load to store energy at the output voltage level. The $100\mu F$ capacitors have a voltage coefficient of 0.61 of their labeled value at 3.3V and 0.47 at 5.25V. The energy harvesting circuit is configured to turn-on at 3.15 V to supply the load and turn-off at 2.25 V.

Figure 3.7 shows the detailed schematic diagram of the LTC3108. The LTC3108 TEG-powered energy harvester is selected by installing the power selection jumper JP2. The board is configured from the factory to use the PGOOD_LTC3459 signal as the PGOOD signal to switch from battery power to energy harvesting power and is available on jumper J8. The PGOOD_LTC3459 signal is always used to switch the output voltage on the header. Some loads do not like to see a slowly rising input voltage. VSUPPLY and VMCU on the headers are off until the energy harvested output voltage is high enough to power the load. The LTC2935-2 is configured to turn on at 3.15V and turn off at 2.25V. With this circuit, the load will see a fast voltage rise at start-up and be able to utilize all the energy stored in the output capacitors between the 3.15V and 2.25V levels.

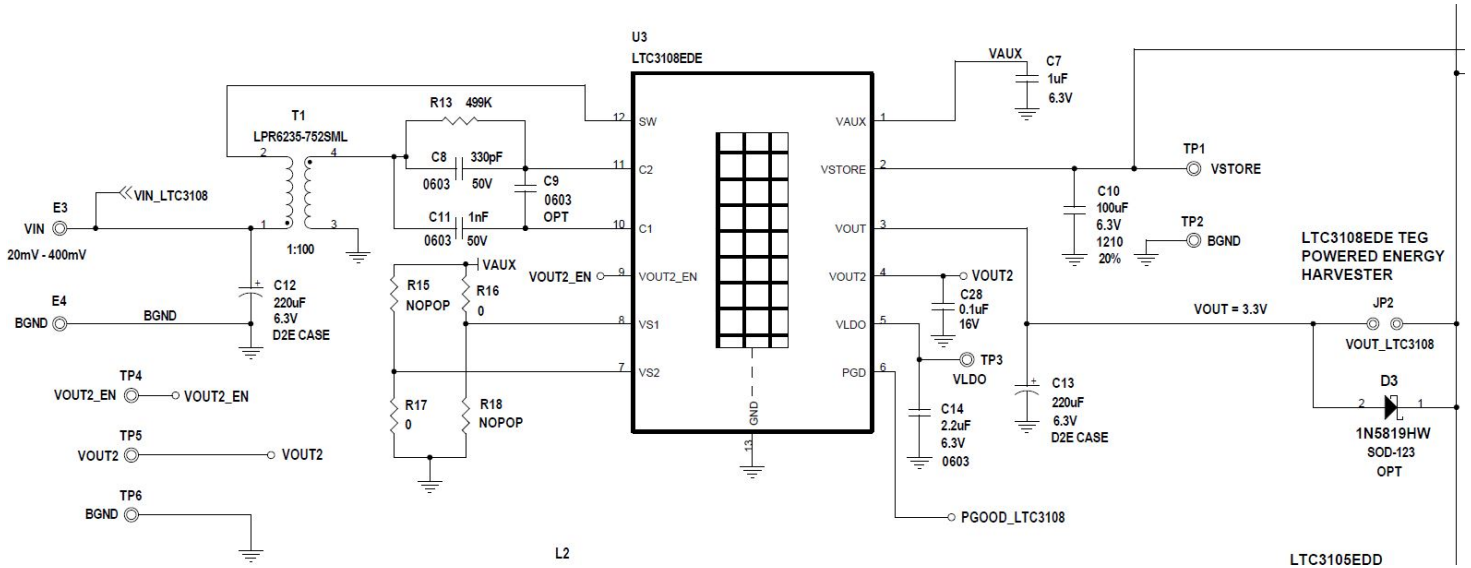

Figure 3.7: Detailed Schematic Diagram of LTC3108 [12]

3.4 WS Node

The prototype that has been developed here will be buried underground for safety & security purposes which require data to be transmitted between nodes through the soil. RF transmission through soil poses many challenges and depends on several factors such as transmission frequency, burial depth, soil dielectric properties, etc. To come up with the best solution for this particular application, studies were conducted on different low power wireless network technology such as Zigbee, Wifi, GSM and NB-IoT, etc. along with practical implementation and underground signal strength tests at different depths. Many of this setup requires setting up a manager node as well to collect store data on a continuous basis. For the purpose of this project we have implemented and tested following three wireless sensor nodes:

- **DC9018B-B Evaluation/Development Mote**
- **Arduino MKR WiFi 1010**
- **Arduino MKR GSM 1400**

3.4.1 DC9018B-B Evaluation/Development Mote

Figure 3.8 shows the DC9018B-B [14] Eterna Evaluation & Development Mote which is an ultra low power wireless device. The mote incorporates the RF-Certified LTP5902-IPM [15] SmartMesh IP Mote PCB Module and performs the functions of sending and receiving sensor data and routing wireless packets. This dust mote is directly compatible with DC2042A EH board. DC9018B-B uses SmartMesh IP technology which is based upon the wireless 2.4 GHz IEEE 802.15.4e [29] standard. According to an amendment published in 2012, IEEE 802.15.4e replaces the MAC protocol of IEEE 802.15.4[5] to adopt the core ideas of time synchronization, time slotting and channel hopping. The core of the IEEE 802.15.4e Times Slotted Channel Hopping (TSCH) mode is that all the motes in the network are synchronized to the same time base. Time is sliced up into time slots, and a communication schedule instructs each mote what to do in each slot: transmit, receive, or sleep.

The schedule is being built in such a way that communication is collision-free, i.e. two pairs of motes will never transmit at the same time, or at the same frequency, resulting in potentially full utilization of the available bandwidth. To combat multipath fading and external interference, motes “channel hop”. That is, each time mote A sends a packet to

Figure 3.8: DC9018B-B Wirelss Node [14]

mote B, it may do so on a different frequency. This means that, if communication is not possible at a given frequency (e.g. because of multi-path fading), the second attempt has a high chance of succeeding since it uses a different frequency. Together, time synchronization and channel hopping allow motes to operate for multiple years on a single battery while having an end-to-end delivery ratio of over 99.999% [17].

Figure 3.9 shows the DC2274A-A USB demo board which serves as the network manager for a SmartMesh IP wireless sensor network shown in figure 3.10. DC2274A-A SmartMesh IP USB Manager incorporates the LTP5902-IPM SmartMesh IP Module, running EManager firmware with 100 mote network capacity, and provides a USB connection for both power and software access to the manager API UART and CLI UART ports.

SmartMesh IP Manager has several key roles in a network. [39]

- The first task of the SmartMesh IP Manager is to build a schedule that accommodates the motes' traffic requirements while staying as "sparse" as possible to keep the mote's energy consumption low.
- The second task of the SmartMesh IP Manager is to maintain the communication in the network flowing when topological changes happen.
- The third task of the SmartMesh IP Manager is to connect the SmartMesh IP network to the outside world.

Figure 3.9: DC2274A-A USB Demo Board

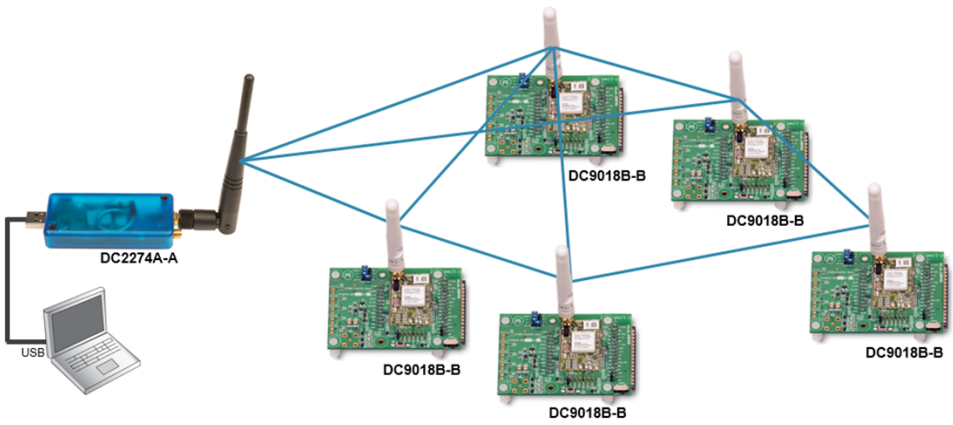

Figure 3.10: Mesh Network [14]

Power consumption analysis of DC9018B-B

Figure 3.11 demonstrates the energy requirements of the sensor node. During the start-up (booting and network discovery), the node consumes on average 17.85 mW and draws current around 6 mA from the source. For the other operations (send, receive, sleep, listen, and standby), the average power consumption is around 0.25 mW and the drawn current is about 0.10 mA. The WS node takes about 5 to 40 seconds to start-up and connects to the sink node. In these experiments, the prototype board is powered using a DC power supply.

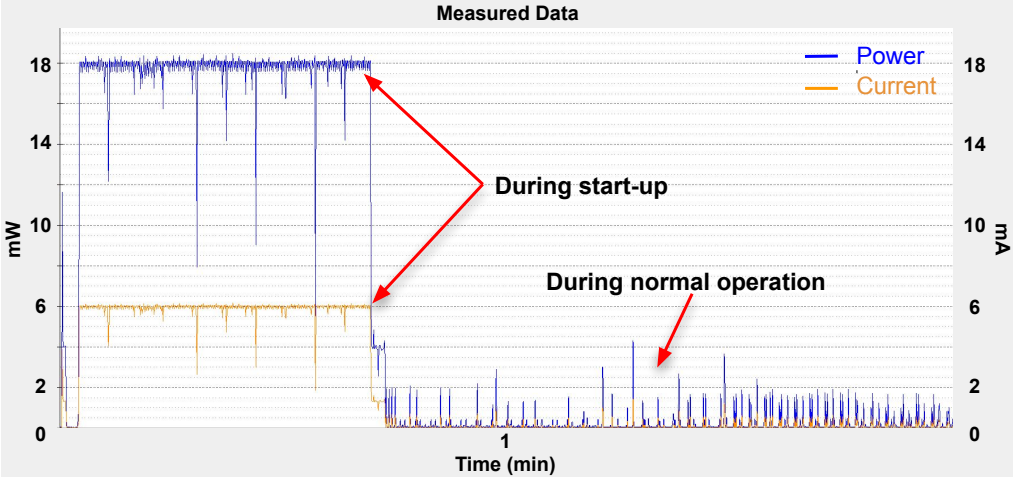

Figure 3.11: Power & current consumption of the sensor node DC9018B-B.

Underground signal strength test of DC9018B-B

RF signal attenuates with burial depth. To find out the maximum burial depth achievable with reliable communication between the sensor node & the manager, several tests were carried out at different burial depths and Received Signal Strength Indicator (RSSI) were measured.

At first, the WS node is placed in a waterproof container (see figure 3.12) and then placed in a storage bin with an almost equal amount of soil at each side as depicted in figure 3.13. 6" of soil is placed under the module to ensure that the RF signal needs to penetrate the same length from any possible angle. During the tests, the module was powered from a coin cell battery and it was programmed to report the RSSI to the Manager as shown in figure 3.14.

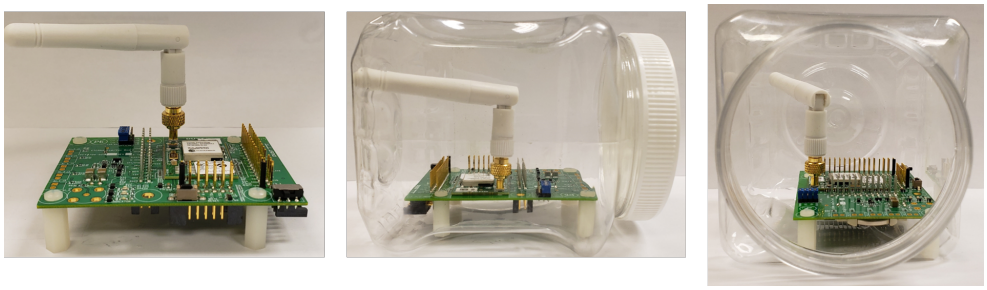

Figure 3.12: Placement of Sensor Node in the Container

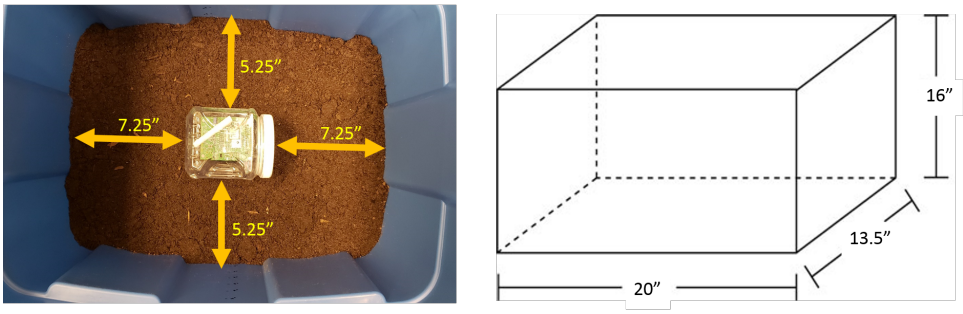

Figure 3.13: Placement of Sensor Node in the Storage Bin

```
show mote 2
Mote #2, mac: 00-17-0D-00-00-31-55-1F
   State:   Oper, Hops: 1.1, Uptime:    7-01:31:02, Age: 7 (*)
   Regular. Route/TplgRoute.
   Power Cost: Max 65534, FullTx 110, FullRx 65
   Capacity links: 200, neighbours 31
   Number of neighbors (parents, descendants): 1 (1, 1)
   Bandwidth total / mote exist (requested):  7557 / 7557 (8637)
       Links total / mote exist (requested):  0.8 / 0.8 (0.7)
       Link Utilization                    :  0.4
   Number of total TX links (exist / extra):  2 / 0
   Number of links      : 9
     Compressed         : 5
     Upstream   tx/rx   : 2 (2/0) (Rx10=0.0)
     Downstream rx      : 2
   Neighbors:
      -> # 1 Q: 87% RSSI: -54/0
```

Figure 3.14: Wireless Sensor Node 1” under soil

Table 3.1 shows the signal strength of DC9018B-B at different burial depths. For this test, the WS node and the manager were kept at a distance of 3m. At a distance of 3m from the manager node, the DC9018B-B mote was able to successfully send and receive data till it was buried 4" underground. At 5" burial depth, the node was establishing a connection with the manager intermittently. At 6" burial depth, the connection was totally lost with the manager.

Table 3.1: Signal strength of DC9018B-B at different burial depth

Module	Frequency Band	Distance	Depth	Signal Strength
DC9018B-B	2.4GHz	3m	1"	-54 dBm
			3"	-70 dBm
			4"	-89 dBm
			6"	Connection Lost

Discussion

Even though DC9018B-B has significantly low power consumption but the burial depth and communication distance is a major drawback. For the application under consideration, burial depth needs to be at least 6 inches and the communication distance between two nodes needs to be at least 100 meters. So DC9018B-B is not suitable for this particular application.

3.4.2 Arduino MKR WiFi 1010

Arduino MKR WiFi 1010 [3] board provides reliable & cost-effective solution for Wi-Fi connectivity. This board is equipped with an ESP32 module made by U-BLOX and is composed of following three main blocks:

- SAMD21 Cortex-M0+ 32bit low power ARM MCU
- U-BLOX NINA-W10 Series low power 2.4GHz IEEE® 802.11 b/g/n Wi-Fi
- ECC508 CryptoAuthentication

Wireless Local Area Network (WLAN) is based on IEEE 802.11 [10] standard and is also known as Wi-Fi. popular extensions of 802.11 specifications are 802.11b, 802.11a, 802.11g and 802.11n.

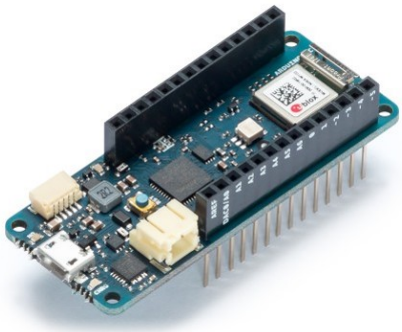

Figure 3.15: Arduino MKR WiFi 1010

Devices that connect to the Wi-Fi network are called stations. Connection to Wi-Fi is provided by an Access Point (AP), that acts as a hub for one or more stations. The AP on the other end is connected to a wired network. An AP is usually integrated with a router to provide access from Wi-Fi network to the internet. Each access point is recognized by a Service Set Identifier (SSID), which essentially is the name of the network you select when connecting a device (station) to the Wi-Fi.

Power consumption analysis of MKR WiFi 1010

Figure 3.17 demonstrates the current and power requirements of the WiFi sensor node. During the start-up (booting and network discovery), the node consumes on average 600

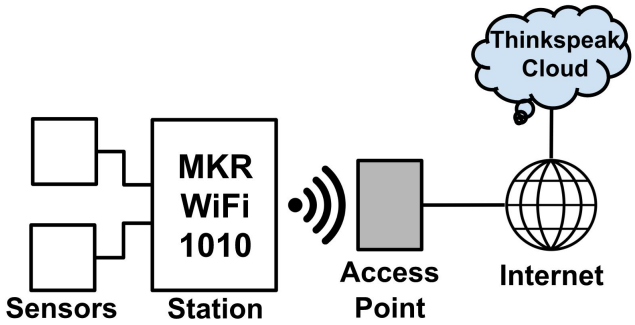

Figure 3.16: Arduino MKR WiFi 1010 operating in station mode

mW and draws current around 120 mA from the source. For the other operations (send, receive, sleep, listen, and standby), the average power consumption is around 210 mW and the drawn current is about 42 mA. The WS node takes about 20 to 40 seconds to start-up and connects to a AP. In these experiments, the prototype board is powered using a DC power supply.

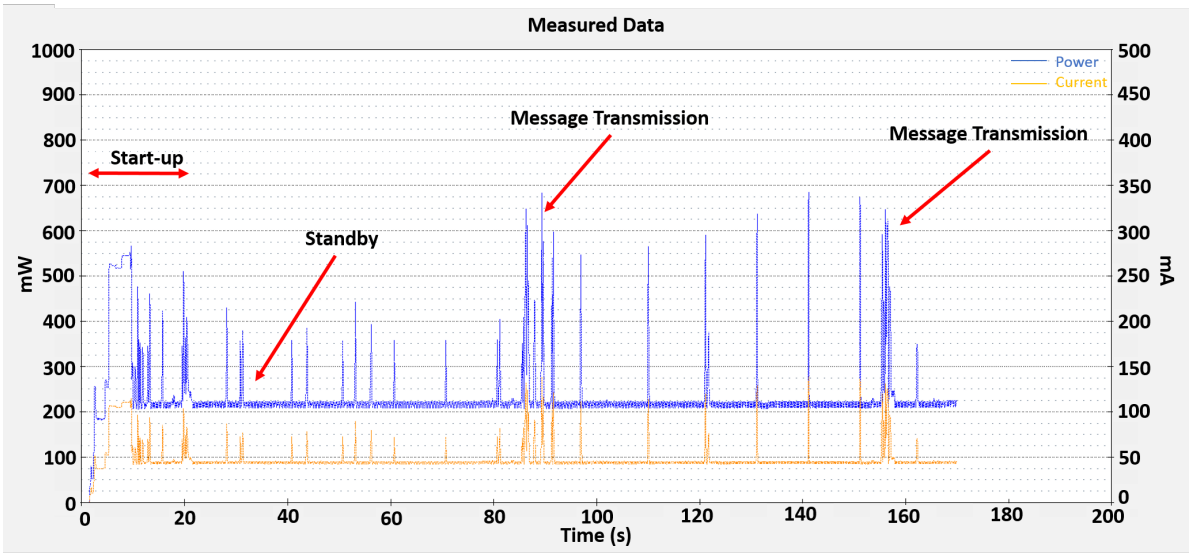

Figure 3.17: Power & current consumption of MKR WiFi 1010

Underground signal strength test of MKR WiFi 1010

Table 3.2 shows received signal strengths for MKR WiFi 1010 at different burial depths. A similar setup as described in section 3.4.1 has been used to conduct the experiments. During the tests, the module was powered from a DC source and it was programmed to report the RSSI to the cloud as at certain intervals. The reported data to the cloud is shown in figure 3.18.

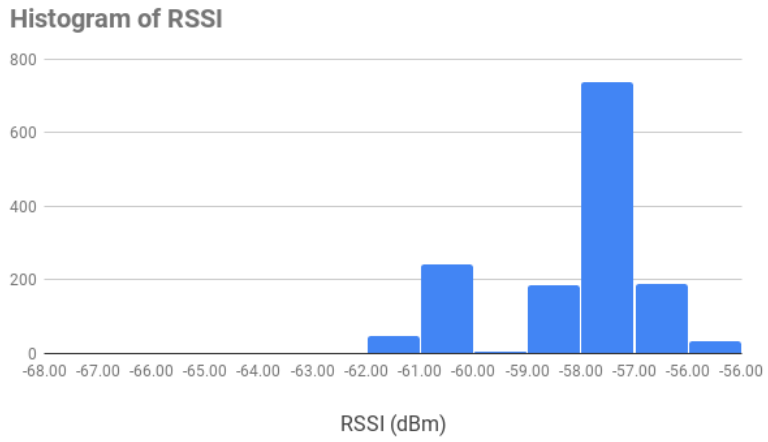

Figure 3.18: Histogram of received signal strength at 1" under soil

Table 3.2: Signal strength of MKR WiFi 1010 at different burial depth

Module	Frequency Band	Distance	Depth	Signal Strength
MKR WiFi 1010	2.4GHz	10m	1" 2" 4" 6"	-58 dBm -72 dBm -76 dBm Connection Lost

Discussion

With MKR WiFi 1010 the communication and data transfer rate increased significantly but the burial depth remains the same as DC9018B-B. Another drawback of MKR WiFi 1010 is the power consummation which increased significantly over the DC9018B-B module.

3.4.3 Arduino MKR GSM 1400

Figure 3.2 shows the Arduino MKR GSM 1400 [2] which uses the cellular network to communicate to the cloud. The GSM / 3G network covers the majority percentage of the world's surface area, as a result, this makes the connectivity option very attractive and easy where there is no other alternative exists. The MKR GSM 1400 can work as a standalone device without the need of any manager or AP. The device gets connected to the internet over 3G as depicted in figure 3.20. The board comes with a low power Arm® Cortex®-M0 32-bit SAMD21 processor and the GSM / 3G connectivity is achieved using the module from u-blox called the SARA-U201 which is a low power chipset operating in different bands of the cellular range such as GSM 850 MHz, E-GSM 1900 MHz, DCS 1800 MHz, PCS 1900 MHz.

Figure 3.19: Arduino MKR GSM 1400

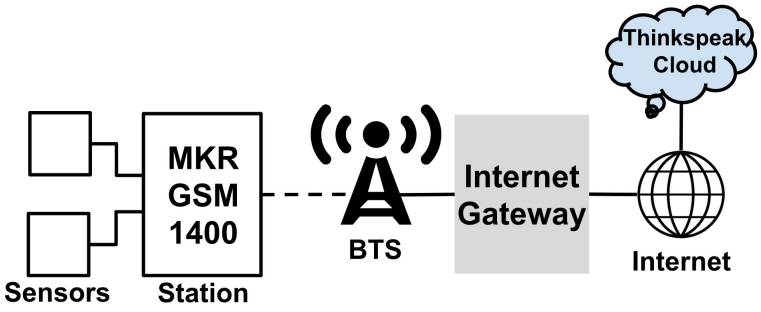

Figure 3.20: MKR GSM 1400 connects to Internet over 3G

Power consumption analysis of MKR GSM 1400

Figure 3.21 demonstrates the energy requirements of the MKR GSM 1400 module. During the start-up (booting and network discovery), the maximum power consummation is around 760 mW and draws current around 310 mA from the source. Transmission of a message requires approximately 10 secs and the power consumption is almost the same. During standby conditions, the average power consumption is around 200 mW and the drawn current is about 80 mA. The WS node takes about 20 to 25 seconds to start-up and connects to a Base Transceiver Station (BTS) node. In these experiments, the prototype board is powered using a DC power supply.

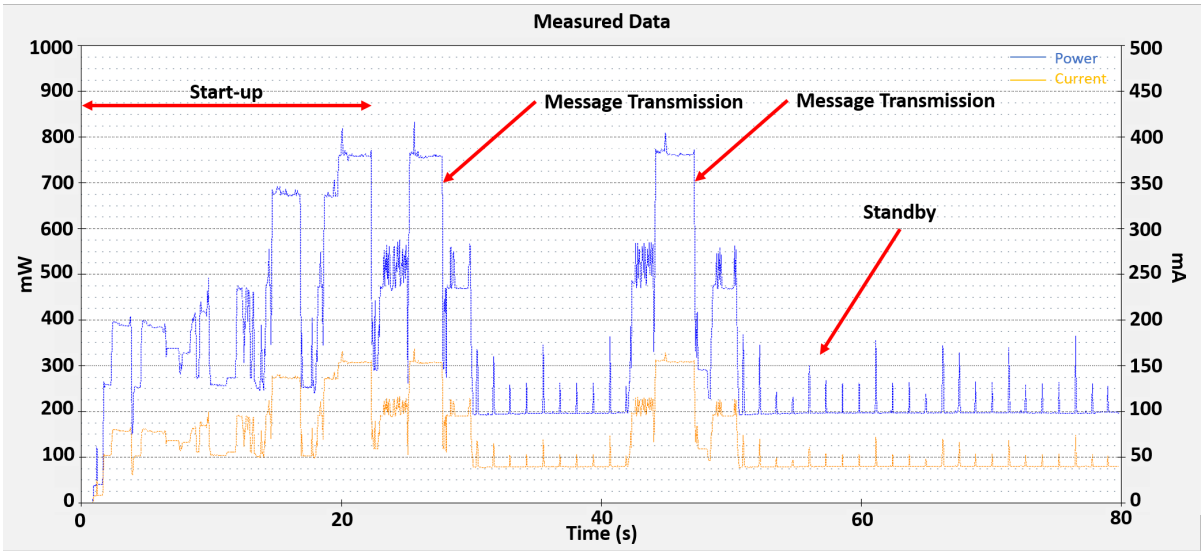

Figure 3.21: Power & current consumption of MKR GSM 1400

Underground signal strength test of MKR GSM 1400

Table 3.3 shows received signal strengths for MKR GSM 1400 at different burial depths. The signal strength is measured on a scale of 0 to 31, where 31 represents excellent signal strength and 0 represents the weakest. A similar setup as described in section 3.4.1 has been used to conduct the experiments except all tests were carried outdoor whereas the previous tests were conducted inside the lab. During the tests, the module was powered using anUniversal Serial Bus (USB) power bank and it was programmed to report the

signal strength data to the cloud at certain intervals. The reported data to the cloud is shown in figure 3.22.

Table 3.3: Signal strength of MKR GSM 1400 at different burial depth

Module	Frequency Band	Range	Depth	Signal Strength
MKR GSM 1400	880MHz	-	Open Air 1” 2” 6”	25/31 20/31 16/31 13/31

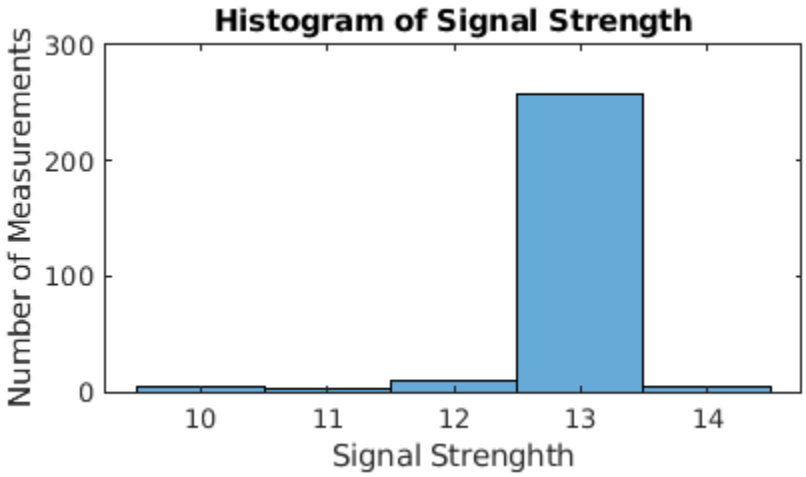

Figure 3.22: Histogram of received signal strength at 6” under soil

Discussion

MKR GSM 1400 has the advantage of long communication range and can connect directly to BTS without the need for any intermediate node. This is a great advantage as it eliminates the management and power issues of relay nodes. As long as the setup is within a certain network the device is able to transmit data reliably even when buried 6” underground. Once the connection is established the communication is reliable and the data transfer rate is also very high. The drawback of MKR GSM 1400 is the power consummation which is significantly high over the previous two modules.

3.5 Summary

Table 3.4 shows a comparison of the tests we have conducted in previous sections. The modules we have tested for our particular application requires to meet a minimum burial depth of 6" and the range of communication between two nodes needs to be at least 100m. While DC9018B-B module offers significantly low power consumption but fails the depth and range test. On the other, hand MKR WiFi 1010 offers a slightly better range but fails the depth test. MKR GSM 1400 was able to pass the depth test and offers a great range as well but the energy required for this module is significantly higher than the other two. As the reporting frequency is very low for the application under consideration, the MKR GSM 1400 module can be a feasible solution for data communication if the charge control circuit is designed properly.

Table 3.4: Comparison of underground tests

Module	Frequency Band	Range	Max Depth	Max Power	Max Current
DC9018B-B	2.4GHz	3-5m	4"	17.85mW	6mA
MKR WiFi 1010	2.4GHz	10-30m	4"	600mW	120mA
MKR GSM 1400	880MHz	Few KMs	> 6"	760mW	152mA

Chapter 4

Design & Evolution

This chapter reports on the design and development of an underground soil-based WS node that utilizes GSM network for communication. The operation of the overall circuit is explained and the key system parameters are outlined here. This chapter also discusses the overall setup and configuration setting of the proposed prototype.

4.1 System Overview

The general structure of the proposed system is shown in figure 4.1. Solid, dashed and dash-dotted lines represent the flow of energy, I/O control signal, and data paths respectively. The overall system can be divided into five stages:

- **Stage 1: Energy Source**
  In SACP technique, steel structures are protected from natural corrosion by enabling an externally connected anode material to deplete over time. Due to this, there is movement of electrons between the anode and cathode that are buried into the soil. We exploit this movement of electrons to harvest energy.

- **Stage 2: EH Module**
  The EH module collects energy from the movement of electrons. The EH module mainly comprises an ultra-low voltage step-up DC/DC converter, and a storage device. The DC/DC step operates at a very low voltage and can convert them to a usable one i.e 3.15V in this case. The onboard external capacitor together forms the storage for the EH module which is expandable if needed.

- **Stage 3: Voltage Switching & Control**
  The voltage that builds up across the capacitor over time is fed to output pins when it reaches a specified level. The switching of voltage to the output pin is controlled at this stage and it ensures that the sensor node is powered only when the output voltage has reached a specified level. The energy harvesting circuit is configured to turn-on at 3.15 V to supply the load and turn-off at 2.85 V.

- **Stage 4: Voltage Regulation**
  At this stage voltage is brought up to 5V to fed the WS Node. The maximum voltage the EH module provides is 3.15V which is boosted to 5V through a booster circuit. Although with the use of energy the capacitor voltage goes down, the booster circuit helps to maintain a constant voltage across the node.

- **Stage 5: Sensing & Transmission**
  At this stage data is being sensed through the analog input port of the MKR GSM 1400 module and transmitted after processing. The WS node is responsible for sensing the current $i(t)$ and transmitting the data to the cloud. Once the module is turned on it is programmed to sends data every 20 secs.

4.2 Operation of the proposed system

Detail operation of the proposed system, outlined in figure 4.1 is explained here. V_{S1} is the voltage across the source and V_{S2} is the input voltage to the EH module where $V_{S1} > V_{S2}$ as there is a small voltage drop across the resistor in series which has been placed to measure the current $i(t)$. The micro-controller senses the voltage V_{S1} & V_{S2} respectively, which is the voltage of two ends of a known resistor and runs a function to calculate the current $i(t)$. The measured current data is then reported to the cloud server. V_{C1} is the voltage across the capacitor which has been stepped up from V_{S2} by the EH module. Here, $V_{C2} = V_{C1}$ and based on voltage V_{C2} the the power to the WS node is controlled. The EH module generates a control signal, P_{g1} based on the capacitor output voltage V_{C2}. Figure 4.2 demonstrates the output and the control signal taken from the EH module. When the output voltage of the EH board reaches 3.15 V, the control signal is ON/HIGH and When the output voltage drops below 2.25 V, the control signal is OFF/LOW.

The onboard control allows the capacitor to drain up to 2.25V before it disconnects the load. As a result lot of energy is wasted due to repeated transmission of the same reading as the change in current reading at a particular time is really insignificant. To disconnect

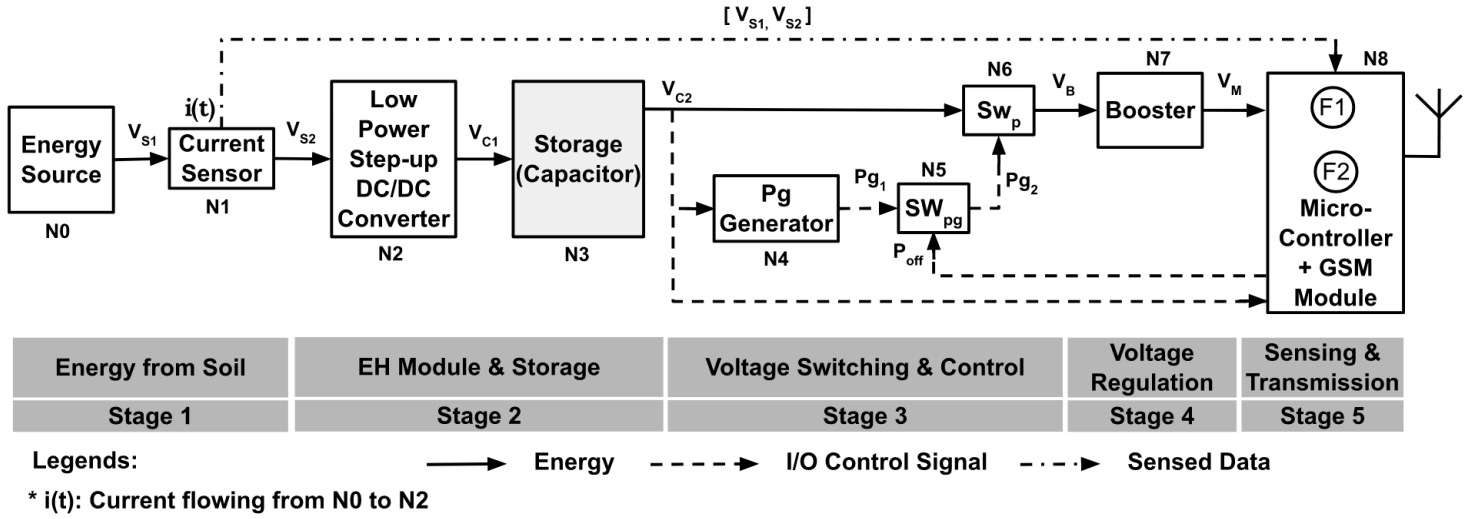

Figure 4.1: Proposed System

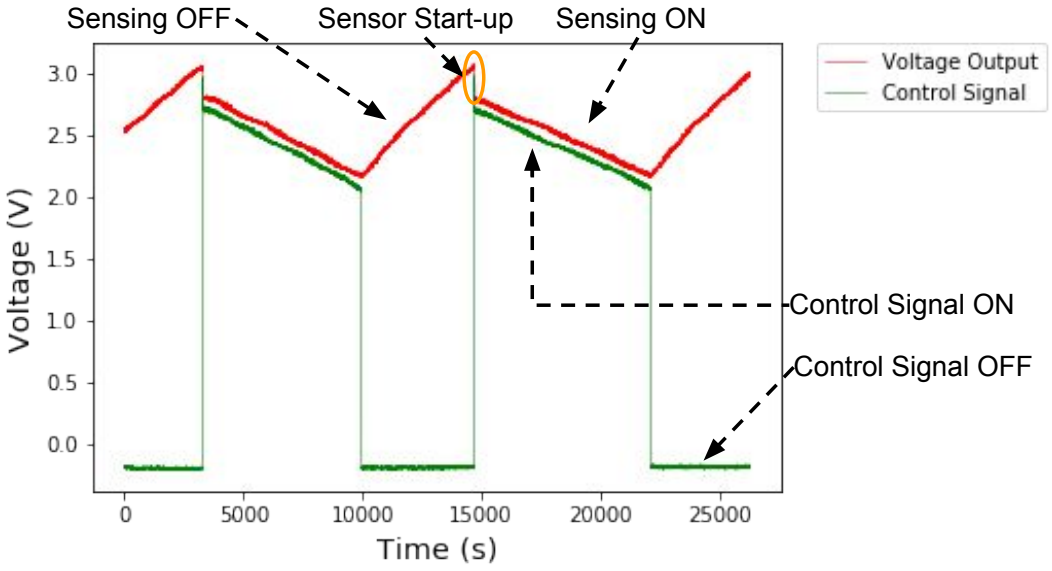

Figure 4.2: The energy harvester's output along with the control signal

the load at a higher voltage and save energy, the additional control circuit has been placed. The circuit is designed in such a way that it disconnects the load after two messages are sent or whenever the capacitor voltage reaches 2.8V. The operation of different switches and function generators are explained below:

- **Operation of P_g Generator**
  $P_{g1} = 1$ if $V_{C2} \geq 3.15V$
  $P_{g1} = 0$ if $V_{C2} \leq 2.25V$

- **Operation of switch SW_{pg}(PGOOD Switch)**
  Initially $P_{off} = 0$
  $P_{g2} = P_{g1}$ if $P_{off} = 0$
  $P_{g2} = 0$ if $P_{off} = 1$

- P_{off} **(Feedback from micro-controller)**
  $P_{off} = 0$ if $3.15V \leq V_{C2} \leq 2.8$
  $P_{off} = 1$ if $V_{C2} < 2.8$

- **Operation of switch SW_p (Power Switch)**
  $V_B = V_{C2}$ if $P_{g2} = 1$
  $V_B = 0$ if $P_{g2} = 0$

- **Operation of Booster**
  $V_M = 5V$ if $3.15V \leq V_B \leq 2.8$
  $V_M = 0V$ if $V_B < 2.8$

The micro-controller implements the following two functions:

Function 1: Calculate $i(t)$ & Send it to thinkspeak cloud server
Input: V_{S1}, V_{S2}, R // Voltage of each end of a known resistor and the value of the resistor
Output: $i(t)$ //Current from energy source
Procedure 1: Calculate $i(t)$

1. Read the analog inputs V_{S1} & V_{S2}
2. Convert analog data to digital voltage V_1&V_2 // $V_1 = V_{S1} * (V_{Ref}/1023)$
3. Calculate the current $i(t)$ // $i(t) = (V_1 - V_2)/R$

Procedure 2:// Data Transmission

1. Initialize ThingSpeak Cloud Server
2. Set the fields with the values
3. Write to the ThingSpeak channel
4. **if x=200**//X=HTTP Status Code
5. channel update successful
6. **else**
7. Error updating the channel

Figure 4.3: Function 1 implemented by the microcontroller

Function 2: Feedback from micro-controller to disconnect the load
Input: V_{C2} // Voltage across the storage capacitor
Output: 0V/5V at digital I/O pin 5// HIGH/LOW
Procedure 1: Monitor Voltage across capacitor

1. Read the analog inputs V_{C2}
2. Convert analog data to digital voltage V_C // $V_C = V_{C2} * (V_{Ref}/1023)$

Procedure 2: Count no. of transmitted message

1. Initiate H=0;
2. **For** Every transmitted message
3. Increment H by 1
4. end **For**

Procedure 3:// Turn digital pin 5 HIGH/LOW

1. initialize digital pin 5 as an output
2. turn digital pin 5 to LOW
3. **if** $(H > 2)$ // H= No. of transmitted message
4. turn digital pin 5 to HIGH
5. wait 5 sec
6. **else**
7. turn digital pin 5 to LOW
8. **if** $(H = 2 \,\&\, V_c < 2.8)$
9. turn digital pin 5 to HIGH
10. wait 5 sec
11. **else**
12. turn digital pin 5 to LOW

Figure 4.4: Function 2 implemented by the microcontroller

4.3 Hardware Implementation

4.3.1 Experimental Setup

The hardware implementation of the proposed system is shown in Figure 4.5. The EH module is realized by the demo board DC2042A [12] from Analog Devices. This board consists of four energy harvesting ICs. For our application, we utilize the energy harvester chip LTC3108 [16]. This chip is an integrated DC/DC converter ideal for harvesting and managing surplus energy from extremely low input voltage sources. The chip can operate from input voltages as low as 20 mV. The WS node is realized by the Arduino MKR GSM 1400 from Arduino. This node connects to the internet using the GSM/3G network and operates in 880 MHz frequency band. The DC-DC booster module is sourced from DFROBOT that can convert voltage between $0.9V \sim 5V$ to standard 5V which is used to power up the GSM module. It integrates a PFM DC-DC boost control chip. A 40F 3.8V supercapacitor along with two MOSFET, LU024N and 18537N have been used for this particular setup. The wiring diagram for the prototype is shown in figure 4.6.

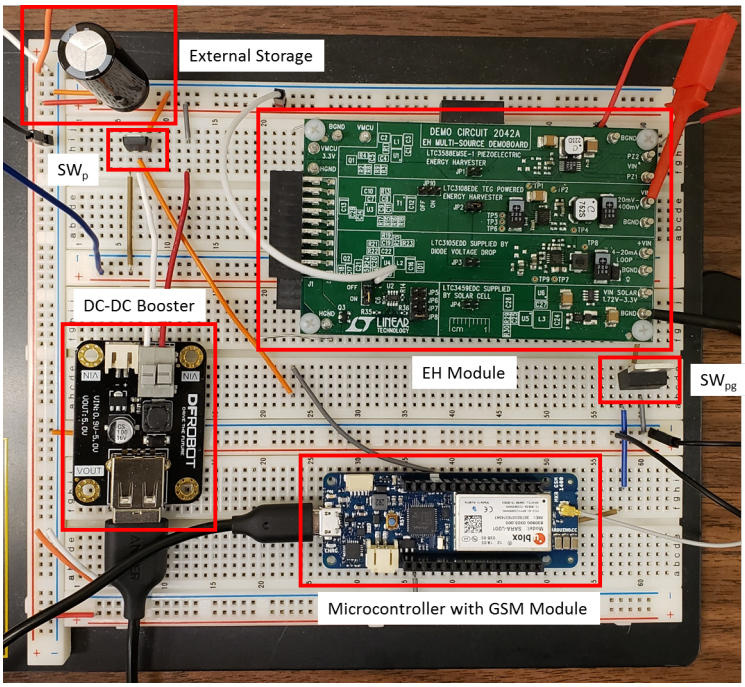

Figure 4.5: The hardware platform of the proposed prototype.

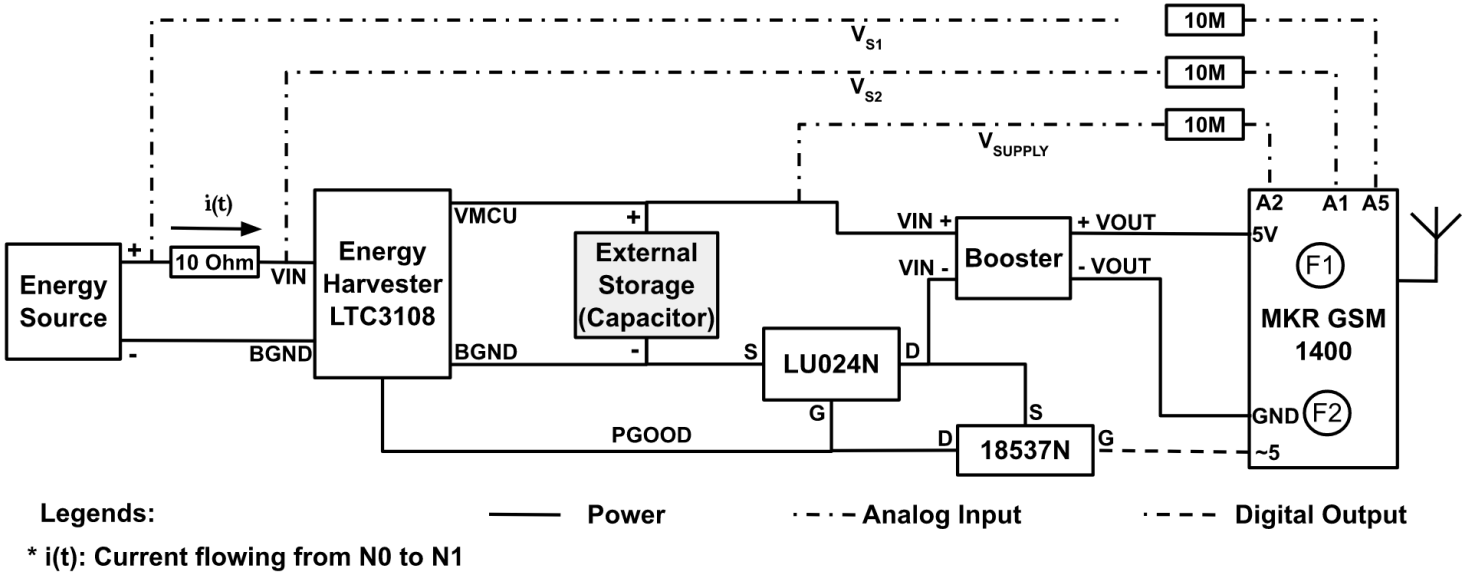

Figure 4.6: Connection Diagram

4.3.2 System Parameters

Key parameters for different devices are outlined below which will be later used for model validation. The open-circuit voltage of the capacitor is approximately 890mv whereas the short circuit current is about 23mA. The voltage across the energy source when connected to the module is 227mV and supplies 12.15mA current. The energy harvester module takes an input voltage of 61mV and charges the capacitors to reach up to 3.15V. There are fifteen optional energy storage capacitors available on-board to be used by the load to store energy at the output voltage level i.e 3.15V. The 100F capacitors have a voltage coefficient of 0.61 of their labeled value at 3.3V and 0.47 at 5.25V. In parallel to those fifteen on-board capacitors, we have added one 40F 3.8V capacitor to meet the energy requirement of the node. The system is designed in such a way that the capacitor will supply power to load when it reaches 3.15V and will disconnect the load when the voltage drops down to 2.8V. During this interval, 2 messages can be sent successfully. The DC-DC booster gets an input voltage in the range of $2.8V \sim 3.15V$ and provides a constant output voltage of 5V to supply the WS Node.

4.3.3 Configuration & Jumper Settings of EH module

Following configuration and jumper settings are required to implement the proposed prototype.

JP2: JP2 power selection jumper is used to select the LTC3108, TEG-powered energy harvester in the EH module.

JP9: Putting jumper JP9 to ON position connects fifteen energy storage capacitors directly to VOUT (VSUPPLY of the Dust Header) to be used by the load to store energy at the output voltage level. Only JP9 or JP10 can be connected at any one time.

JP8: JP8 routes the LTC3459 PGOOD signal to the Dust Header PGOOD output. The board comes pre-configured from the factory to use the PGOOD_LTC3459 signal as the PGOOD signal to switch from battery power to energy harvesting power. We have used this to implement the prototype.

VIN, 20mV to 400mV (E3): Input to the LTC3108, TEGpowered energy harvester. Pin 5 of J4, Vertical Transducer Header can also be used depicted in figure 4.7.

BGND (E4, E6, E8, E11, E14): This is the board ground. Pin 2/4/6/8/10 of J4, Vertical Transducer Header can also be used as depicted in figure 4.7.

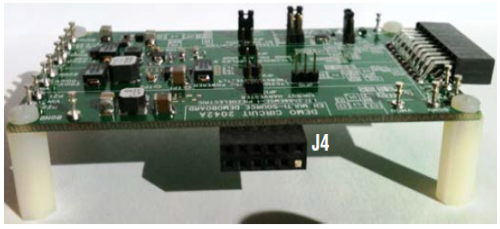

(a) J4,Header

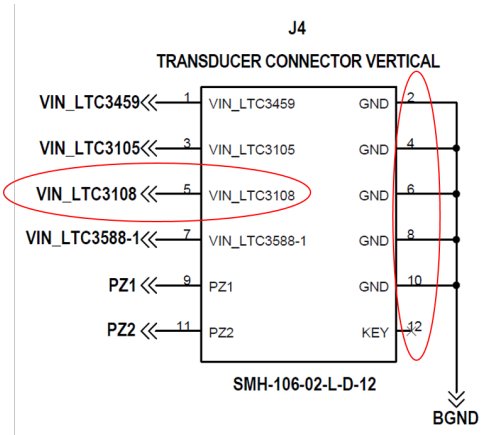

(b) J4, Pinout

Figure 4.7: J4,Vertical Transducer Header

VMCU (E10, E12): Regulated output of all the active energy harvester power management circuits, referenced to BGND.

(PGOOD): PGOOD signal is used to switch the output voltage on the header. PGOOD configured to turn ON at 3.15V and turn OFF at 2.25V. Pin 4 of J2, Dust Mote Header can also be used as shown in figure 4.8.

(VSUPPLY): Switched power from EH multisource demo board. On the board, this node is labeled as VMCU. Pin 1 of J2, Dust Mote Header can also be used as shown in figure 4.8.

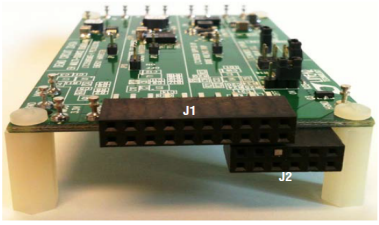

(a) J2, Header

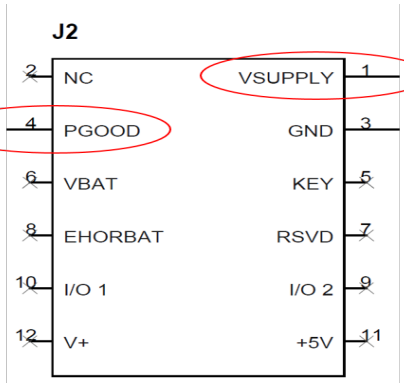

(b) J2, Pinout

Figure 4.8: J2, Dust Mote Header

4.3.4 Underground Deployment

Figure 4.9 (a) & Figure 4.9 (b) shows the implementation of the circuit in a PCB board. The components except the EH module were put into a PCB board and shouldered together to accommodate the entire circuit into a compact box so that the module can be deployed underground.

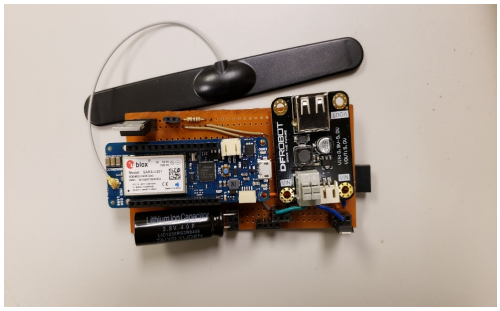

(a) Top view of the circuit

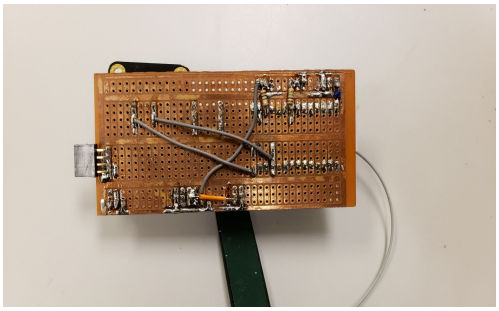

(b) Bottom view of the circuit

Figure 4.9: PCB board implementation

Figure 4.10 (a) shows the prototype placed in a small container of dimension 5.5” x 5.5” x 1.5” for deployment in the soil. To mimic the actual setup environment 6 inches of soil is placed at each side of the container as depicted in figure 4.10 (b). Later, another 6

inches of soil is placed on top of the container. Figure 4.11 shows the overall lab setup of the project.

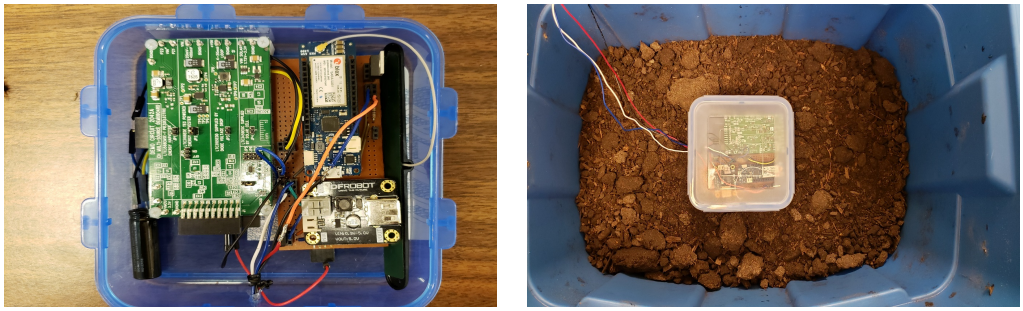

(a) Housing for the circuit board (b) Underground deployment

Figure 4.10: Housing for the prototype

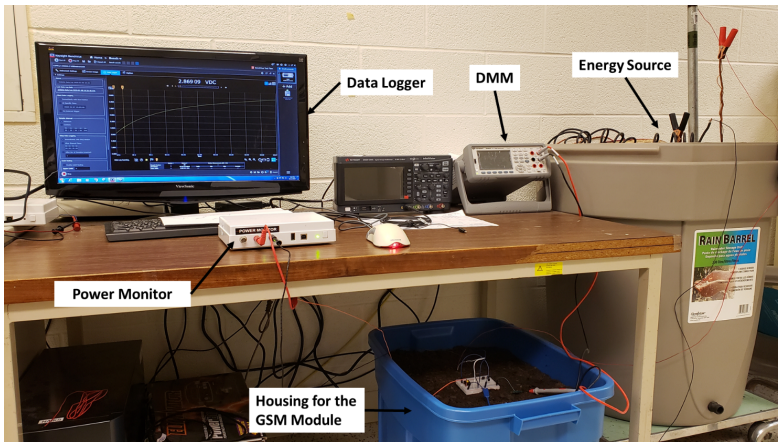

Figure 4.11: Lab setup

4.4 Charging & Discharging Operation

Figure 4.12 shows the charging operation of the capacitor using the energy from the soil. A 40F capacitor requires 1 day and 8 hrs (111600s) to charge from 2.8V to 3.15V. The sharp drop in the voltage from 3.15V to 2.8V is due to the operation of the GSM module.

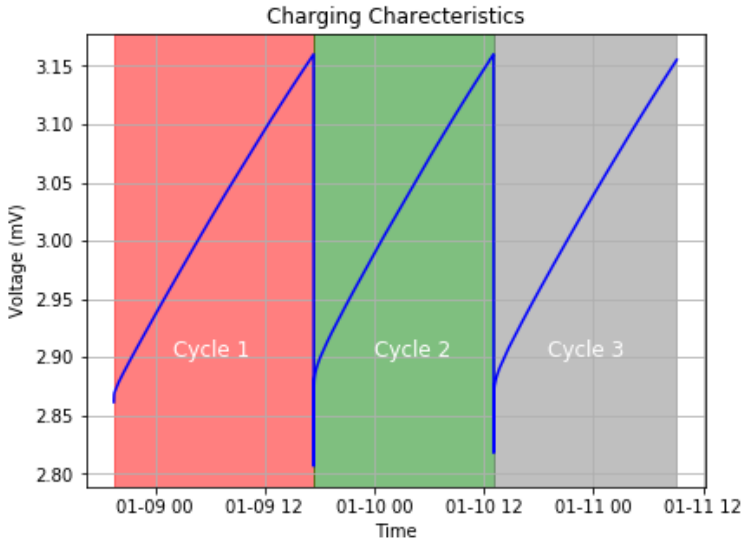

Figure 4.12: Charging Operation

Figure 4.13 shows the discharge operation of the capacitor. The module is programmed to disconnect from the source whenever it sends messages or the capacitor voltage goes below 2.8 V. The sudden sharp voltage drop indicates the message transmission phase. Each message transmission phase lasts approximately 62secs.

Figure 4.14 shows the received messages at the cloud server. Messages get corrupted sometimes due to server issues. As a result, the broad is programmed in such a way that multiple measurements are taken and sent to the cloud to prevent data loss.

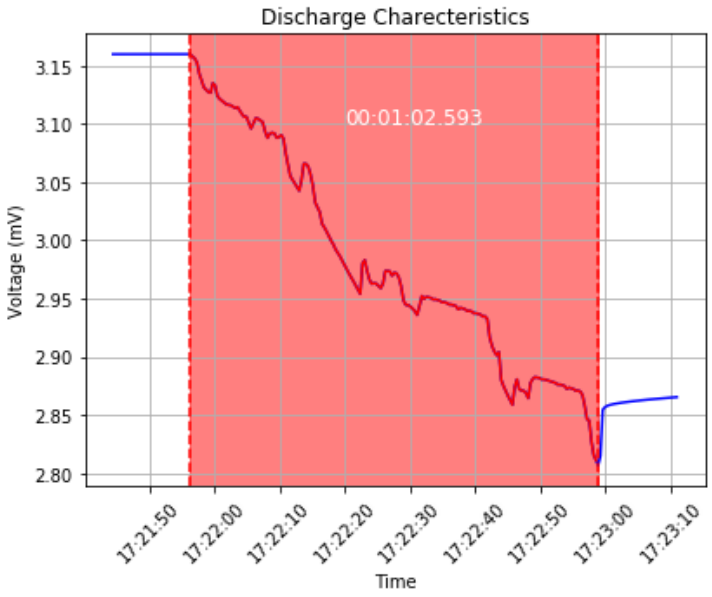

Figure 4.13: Discharging Operation

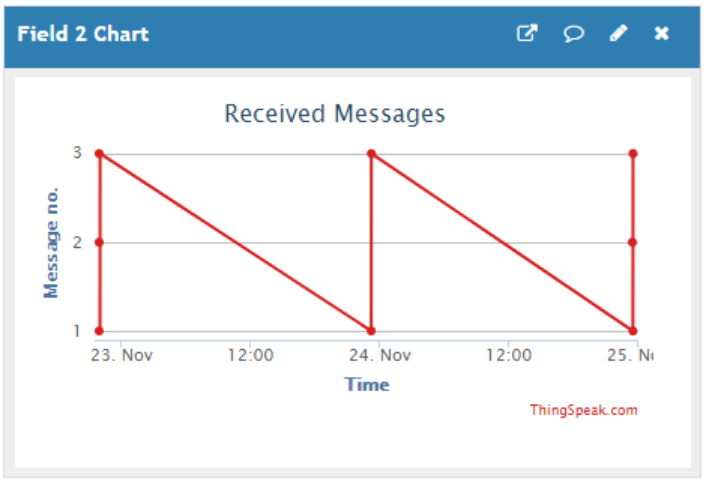

Figure 4.14: Received Messages at the Cloud Server

Chapter 5

Characterization and Modeling of the Energy Source

In this section, we explore the fundamental electric characteristics of the source we have been using to power the sensor node. Several experiments and results are presented here. Based on the results an equivalent circuit model is presented later in this section. The method to calculate different parameters of the equivalent circuit is also discussed.

5.1 Background

Significant development of different renewable energy sources has occurred in recent years and yet there is no perfect solution. Photovoltaic (PV), wind, hydro dominates this market whereas, scientists are still looking for new and innovative solutions every day. Energy harvesting from an SACP setup is such an innovative idea and offers a wide research area. All energy sources are represented by some sort of equivalent circuit [7] or mathematical model to easily understand and solve numerical problems. Characterization and modeling of a soil cell is unique and first of its kind to the best of our knowledge and will help us understand the performance and behavior of the system better.

5.2 Test Setup

The knowledge of the current-voltage characteristic of a soil cell can provide useful insights about its performance. It can also provide information about its operating point and

accordingly necessary changes can be made to produces the maximum power. To find out the current-voltage characteristics of the cell, it needs to be exposed to many different loads. Figure 5.1 shows a test setup for measuring current and voltage to obtain the current-voltage characteristic. Maximum power as the product of power and voltage can be found from the obtained results. The experiments have been conducted by varying resistor across the soil cell and recording current & voltage reading for many different resistor settings as depicted in 5.1.

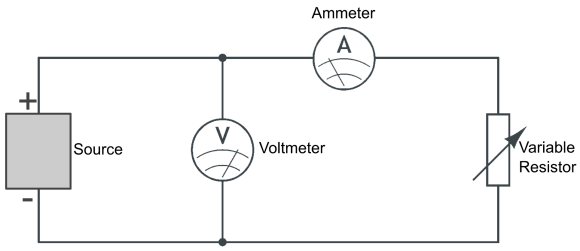

Figure 5.1: Test Setup.

5.3 Characterization of the Soil Cell

5.3.1 Voltage Characteristics

Figure 5.2 shows the circuit setup for the open-circuit test. The voltage of the unloaded circuit is named as V_{OC} and is measured with a voltmeter directly across the soil cell contacts. This is the maximum voltage that the cell is able to provide when there is no load connected i.e. resistance across the cell is infinity.

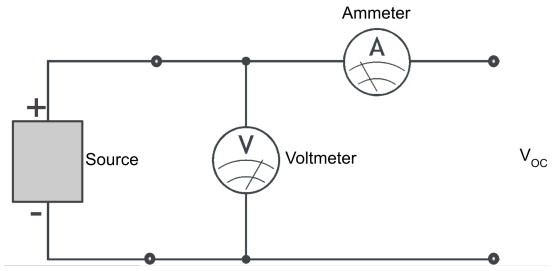

Figure 5.2: Open Circuit Test

Figure 5.3 shows test results for the open-circuit test. From the result, we can observe that the voltage builds up across the terminal is gradual which is due to the accumulation of charge in anode and cathode over time. After a certain time, this accumulation of charge stops and the V_{OC} reaches a stable value. This phenomenon has a resemblance to capacitor charging behavior. The x-axis is presented in seconds which shows that it took almost a day (84000s) to reach a stable voltage.

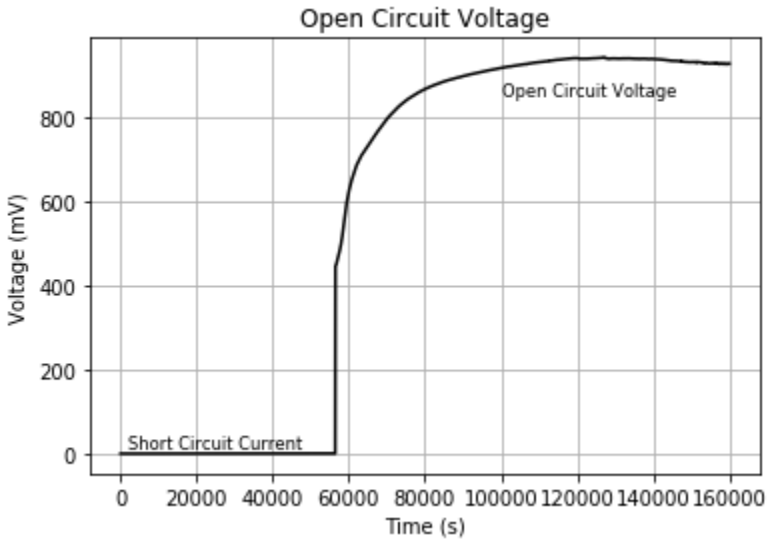

Figure 5.3: Open Circuit Voltage

Figure 5.4 shows the Voltage vs Time characteristics of the cell where voltages where recorded for a certain period of time for different resistor settings. All these tests were carried out after the open-circuit voltage V_{OC} is reached. From figure 5.4 we can see that there is a transient state at the beginning of each graph and later the voltage got steady. The initial voltage drop is due to the capacitance formation across anode & cathode and disappears within a few hundred seconds(500 700) depending on the connected load.

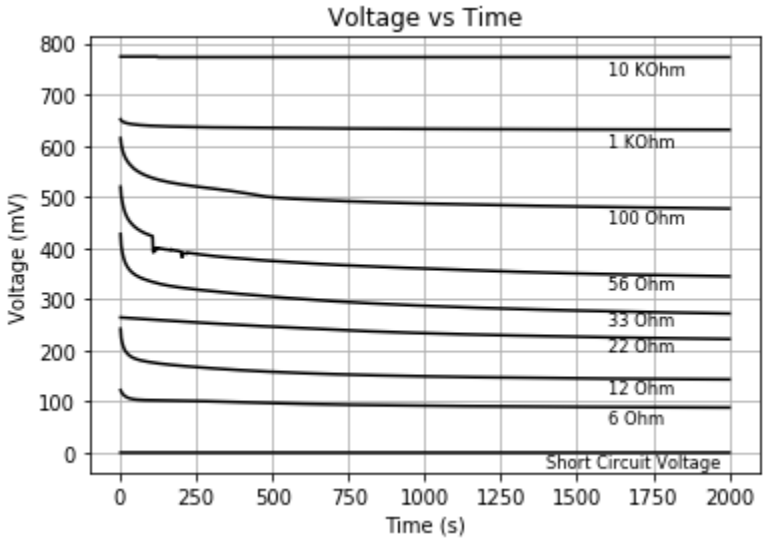

Figure 5.4: Voltage vs Time Characteristics.

5.3.2 Current Characteristics

Figure 5.5 shows the circuit set up for the short circuit test. With the increase of load, the resistance across the cell decreases and as a result, the voltage keeps decreasing until it reaches the short-circuit condition. At short-circuit condition the voltage across the cell is zero. The situation reached by infinite load across the cell is the short circuit of the system and is precisely the state when the ammeter reading is recorded. The short circuit current measured is termed as I_{SC} and is the maximum current that the source can deliver.

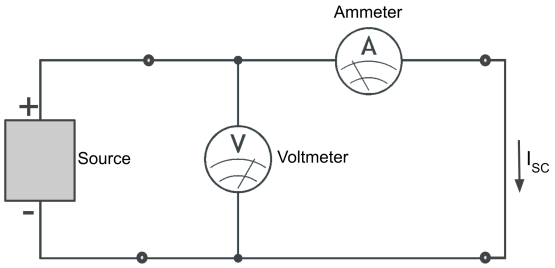

Figure 5.5: Short Circuit Test

Figure 5.6 shows the short-circuit characteristics of the source. There is an initial high current for a few seconds due to the capacitance, that builds up across the anode and the

cathode when it is kept at the open-circuit condition. The current gradually settle down over time and comes to a stable condition. The short-circuit current when it reaches a stable condition varies around 21mA to 22 mA.

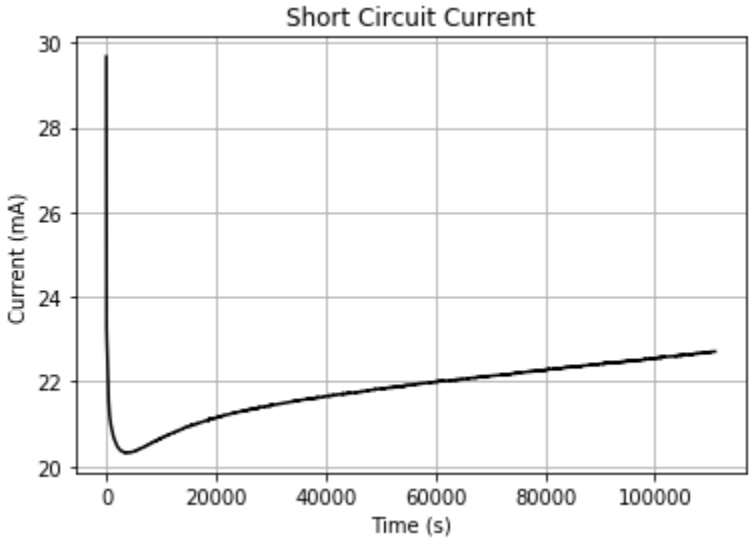

Figure 5.6: Short Circuit Characteristics.

Figure 5.7 shows the Current vs Time characteristics of the cell where the current was for a certain period of time for different resistor settings. All these tests were carried out after the open-circuit voltage V_{OC} is reached. From figure 5.7 we can see that there is a transient high current at the beginning of each graph and later the current got steady. The initial high current is due to the high voltage that accumulates due to the capacitance formation across anode & cathode. This disappears within a few hundred seconds(500 700) depending on the connected load.

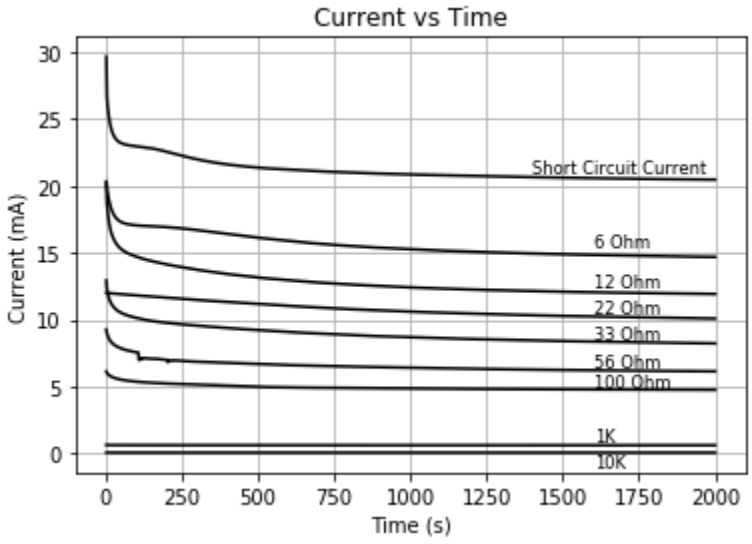

Figure 5.7: Current vs Time Characteristics.

5.3.3 I-V Characteristics

The I-V characteristic of the source is a plot of all possible working points in a considered range. The current and voltage measured under stable conditions are used to generate the plot. Figure 5.8 shows the I-V characteristic of the source. The blue dots represent the measured data from field trials and the red solid line represents the best fit for these dots. The straight line represents that the circuit is resistive in nature and follows ohm's law [41].

$$V = I \times R \tag{5.1}$$

The graph also suggests that the source used here is a DC source, as when $R = 0$, $V = 0$ and when $R = inf$, $V = V_{max}$ and follows eqn. 5.1 for any other value of R. This clearly indicates that the source is a DC source with a resistance in series.

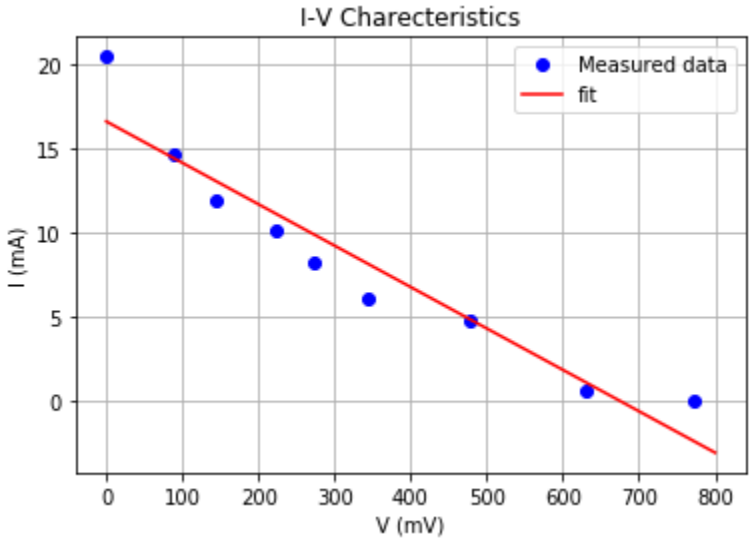

Figure 5.8: I-V Characteristics.

5.3.4 P-V Characteristics

Figure 5.9 shows the P-V characteristics of the source. The P-V characteristic is obtained by finding the power dissipation (i.e product of current & voltage) for a particular resistor setting and plotting it against the voltage data.

$$P = I \times V \tag{5.2}$$

There is one combination of current and voltage at which the power of the soil cell has its maximum (I_{mp} and V_{mp}, respectively). This point on the P-V characteristic is called the Maximum Power Point (MPP) which we can derive from the P-V characteristics.

$$Pmpp = Imp \times Vmp \tag{5.3}$$

The blue dots in the graph represents the power measured for different resistor setting and the solid line represents the best fit for dots. Again the P-V curve indicates that the stable state behavior of the source is purely resistive and the source itself is a DC source.

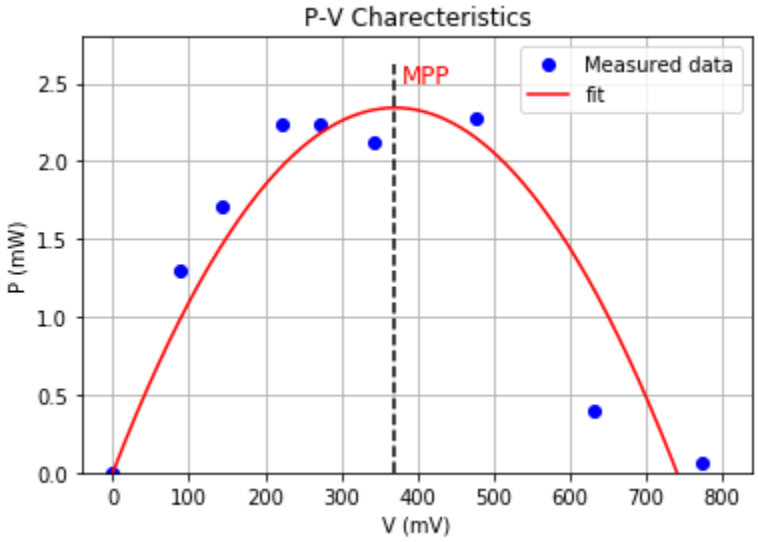

Figure 5.9: P-V Characteristics.

5.4 Proposed Equivalent Circuit Model

Based on the characterization study of the source we can say that the source can be modeled as a DC source with a resistor "R_s" in series. The Series resistance "R_s" is the resistance of the soil. We call it a simplified model of the source and the equivalent circuit is shown in figure 5.10a.

To find the exact model of the source, the transient behavior needs to be addressed. As discussed earlier there is a formation of capacitance due to accumulation of charge across the anode and the cathode. This build of capacitance is across the two materials inside the soil just like resistor "Rs" we have already discussed. This means the soil resistance "R_s" and "C_s" are in parallel with each other and in series with the voltage source. We call this model an exact model of the source as this encounters the initial transient behavior and the equivalent circuit is shown in figure 5.10b.

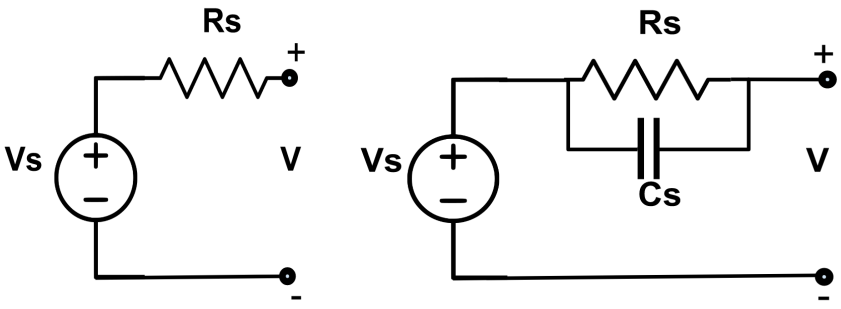

(a) Simplified Model (b) Exact Model

Figure 5.10: Equivalent Circuit Model

5.5 Finding the parameters "R_s" & "C_s"

The model we have discussed in the previous section has two unknown parameters which we can find using the characteristics curves we have obtained earlier.

Parameter "Rs"

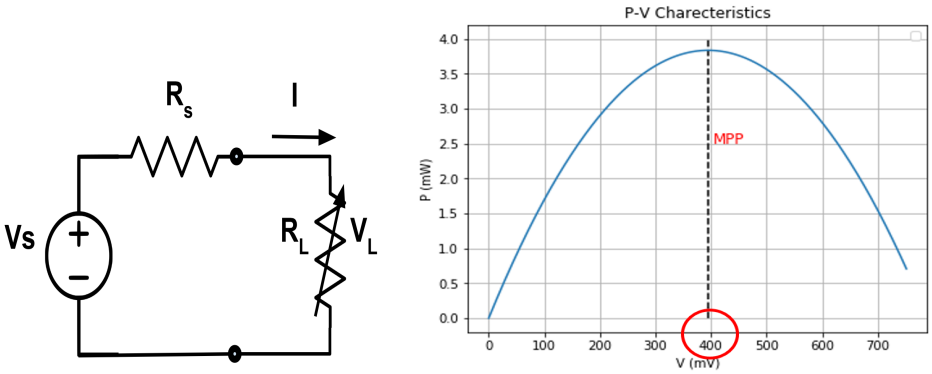

(a) Circuit (b) P-V Characteristics

Figure 5.11: Maximum Power Transfer

From maximum power transfer theorem, we know that the power will be maximum when load resistance equals the source internal resistance. To determine the soil resistance "R_s"

simplified model has been considered. From figure 5.11 (a) we can say that,

$$P = \frac{V_L^2}{R_L} \tag{5.4}$$

let, $P = P_{max}$ and $V_L = V_{max}$ when power is maximum,

$$P_{max} = \frac{V_{max}^2}{R_L} \tag{5.5}$$

According to maximum power transfer theorem, the power will be maximum when $R_L = R_s$. Replacing R_L by R_s we get

$$P_{max} = \frac{V_{max}^2}{R_s} \tag{5.6}$$

Therefore,

$$R_s = \frac{V_{max}^2}{P_{max}} \tag{5.7}$$

From, the P-V (b) characteristics shown in figure 5.11 P_{max} and V_{max} can be easily found and "R_s" can be calculated.

Parameter "C_s"

From capacitor's discharge equation we know,

$$V(t) = V_0 \times e^{\frac{-t}{RC}} \tag{5.8}$$

Here, "$V(t)$" is the voltage across a capacitor at any given time "t", "V_0" is rated voltage of the capacitor and "RC" is the time constant.When "$t = 5RC$",

$$V(t) = V_0 \times e^{-5} \tag{5.9}$$

$$V(t) = V_0 \times 0.006 \tag{5.10}$$

This implies that the voltage across the capacitor is zero after 5 time constant. Considering this, from figure 5.12 we can find the time the voltage took before it got stable. let the time be "Δt". So we can say,

$$\Delta t = 5 \times R_s \times C_s \tag{5.11}$$

Therefore,

$$C_s = \frac{\Delta t}{5 \times R_s} \tag{5.12}$$

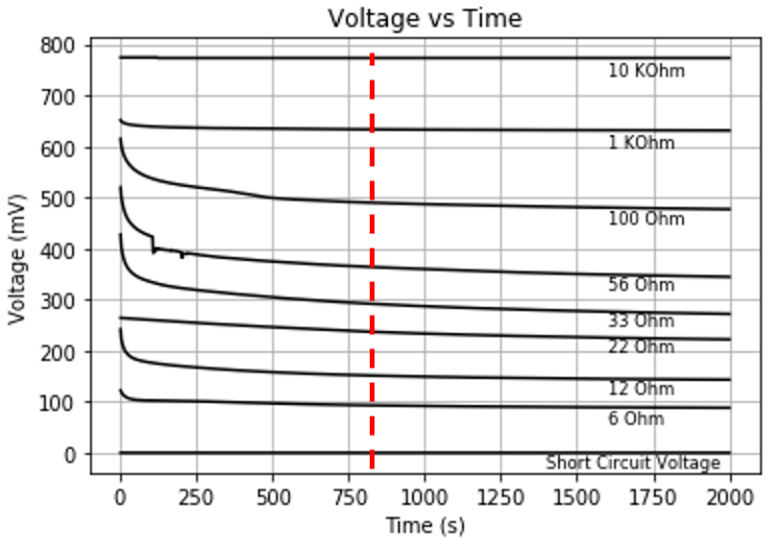

Figure 5.12: Voltage vs Time Characteristics.

5.6 Overall circuit model

Based on the simplified model that we have developed in the earlier section an overall model has been developed which is shown in figure 5.13. The model that has been developed has 2 phases. Figure 5.13 (a) represents the charging model where the source provides power to the capacitor for charging and figure 5.13 (b) shows the discharge model where the capacitor is providing energy to the load. Although when the load is active the charging and discharging of the capacitor happens simultaneously, due to low charging current compared to high discharge current and high charging time compared to low discharge time, the momentary effects can be ignored. With this assumption the proposed model can also give pretty accurate results.

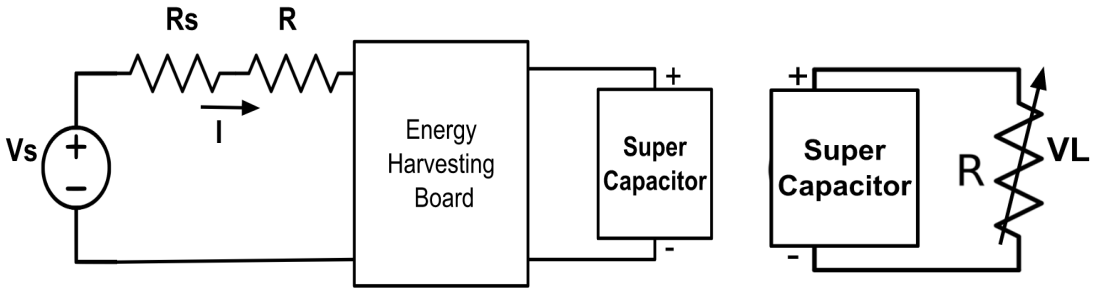

(a) Charging Model (b) Discharging Model

Figure 5.13: Charging & Discharging model

With the assumptions in mind the circuit becomes a straight forward capacitor charging and discharging circuit which can be modeled as follows respectively:

$$V_C(t) = V_0[1 - e^{\frac{-t}{RC}}] \tag{5.13}$$

$$V_C(t) = V_0 e^{\frac{-t}{RC}} \tag{5.14}$$

5.7 Analytical characterization of the charging time

The time T_C required to charge a capacitor from some initial voltage $V_C = V_L$ to a fully-charged state with $V_C = V_H$ is called the charging time.

Voltage V_C across a capacitor is a function of time, So we name V_C as $V_C(t)$. V_C and $V_C(t)$ has the same meaning and has been used interchangeably.

Considering the super capacitor as a conventional capacitor and constant power charging energy E over time t will be $E(t) = P \times t$. Where $P = V(t).I(t) = \frac{q}{c}\frac{dq}{dt}$. Using $q = CV_C$ and solving for V_C we obtain $V_C(t)$ across an initially uncharged supercapacitor at time t,

$$\int_0^{V_C} V_C dV_C = \int_0^t \frac{P}{C} dt \tag{5.15}$$

or,

$$V_C(t) = \sqrt{(\frac{2Pt}{C})} \tag{5.16}$$

From (5.19), current variation with time is obtained as $I(t) = \sqrt{(\frac{PC}{2t})}$. Charging time $T_{V_H}^{ideal}$ for storing Q coulombs of charge (or $V_C(t = T^{ideal} \stackrel{\Delta}{=} V_H)$ accross an initially uncharged supercapacitor is $(V_C(t = 0) \stackrel{\Delta}{=} 0V)$ is given by:

$$T_{V_H}^{ideal} = \frac{C}{P}\int_0^{V_H} V_C dV_C = \frac{CV_H^2}{2P} \tag{5.17}$$

Charging time $T_{V_L}^{ideal}$ for storing Q coulombs of charge (or $V_C(t = T^{ideal} \stackrel{\Delta}{=} V_L)$ accross an initially uncharged supercapacitor is $(V_C(t = 0) \stackrel{\Delta}{=} 0V)$ is given by:

$$T_{V_L}^{ideal} = \frac{C}{P}\int_0^{V_L} V_C dV_C = \frac{CV_L^2}{2P} \tag{5.18}$$

Difference in eqn. (5.17) eqn. (5.18) gives the charging time T_C to charge a capacitor from some initial voltage $V_C = V_L$ to a fully-charged state with $V_C = V_H$.

$$T_C = T_{V_H}^{ideal} - T_{V_L}^{ideal} \tag{5.19}$$

Chapter 6

Validation

In the previous chapter, we have proposed the equivalent circuit model for the source and showed the techniques to find different parameters of the model. In this chapter, we will validate our proposed model with field data and find out the accuracy of the proposed model.

6.1 Validation Technique

To validate the proposed model, first, different parameters of the equivalent circuit are calculated following the steps explained in chapter 5. For the calculation of these parameters, field trial data are used. Then a similar circuit has been created in MATLAB Simulink and results were obtained. Both the field trial data and simulation data have been compared and used to find the accuracy of the model.

6.1.1 Finding parameter "R_S" & "C_s"

From eqn. 5.7 eqn. 5.12,

$$R_s = \frac{V_{max}^2}{P_{max}} \tag{6.1}$$

$$C_s = \frac{\Delta t}{5 \times R_s} \tag{6.2}$$

Data obtained from field trials shows V_{max}=370.7mV , P_{max}=2.34 mW and $\Delta t = 750s$, which gives $R_s = 58.67ohm$ and $C_s = 2.6F$. The open

Based on the values obtained above, a MATLAB Simulink model has been created and "Voltage vs Time" and "Current vs Time" graphs were obtained. Figure 6.1 shows the MATLAB Simulink model which has been used for simulation.

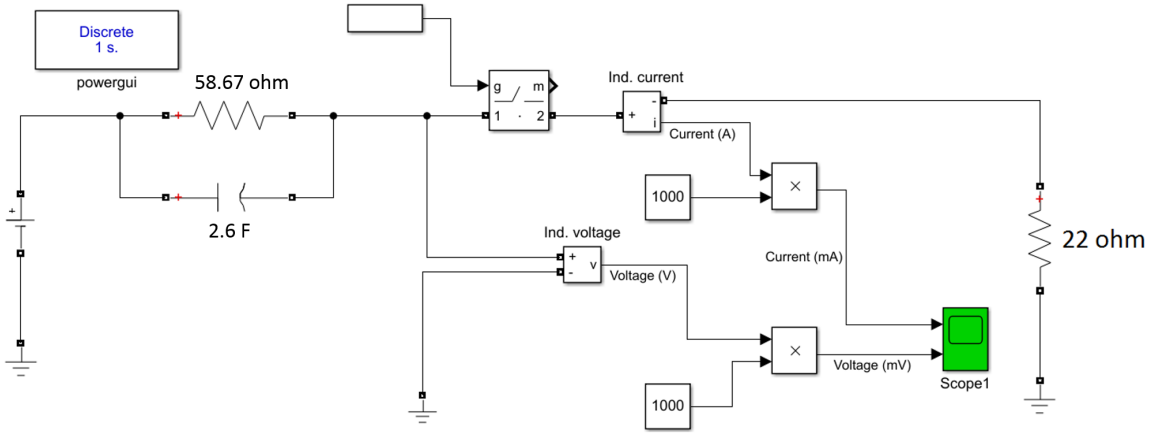

Figure 6.1: MATLAB Simulation Model

The simulation results are presented in figure 6.2. The simulation results show a very close resemblance to the ones obtained from the field trials. Table 6.1 & 6.2 shows the error percentage of the model by comparing the measured data from field trials with the simulation data.

Table 6.1: Comparison of voltage (mV) from field trial & simulation

Resistor(ohm)	Data from field trial	Data from simulation	Error %
6	98	95	3.06
22	225	230	-2.2
56	400	430	-7.5
100	500	560	-12
1000	675	800	-18

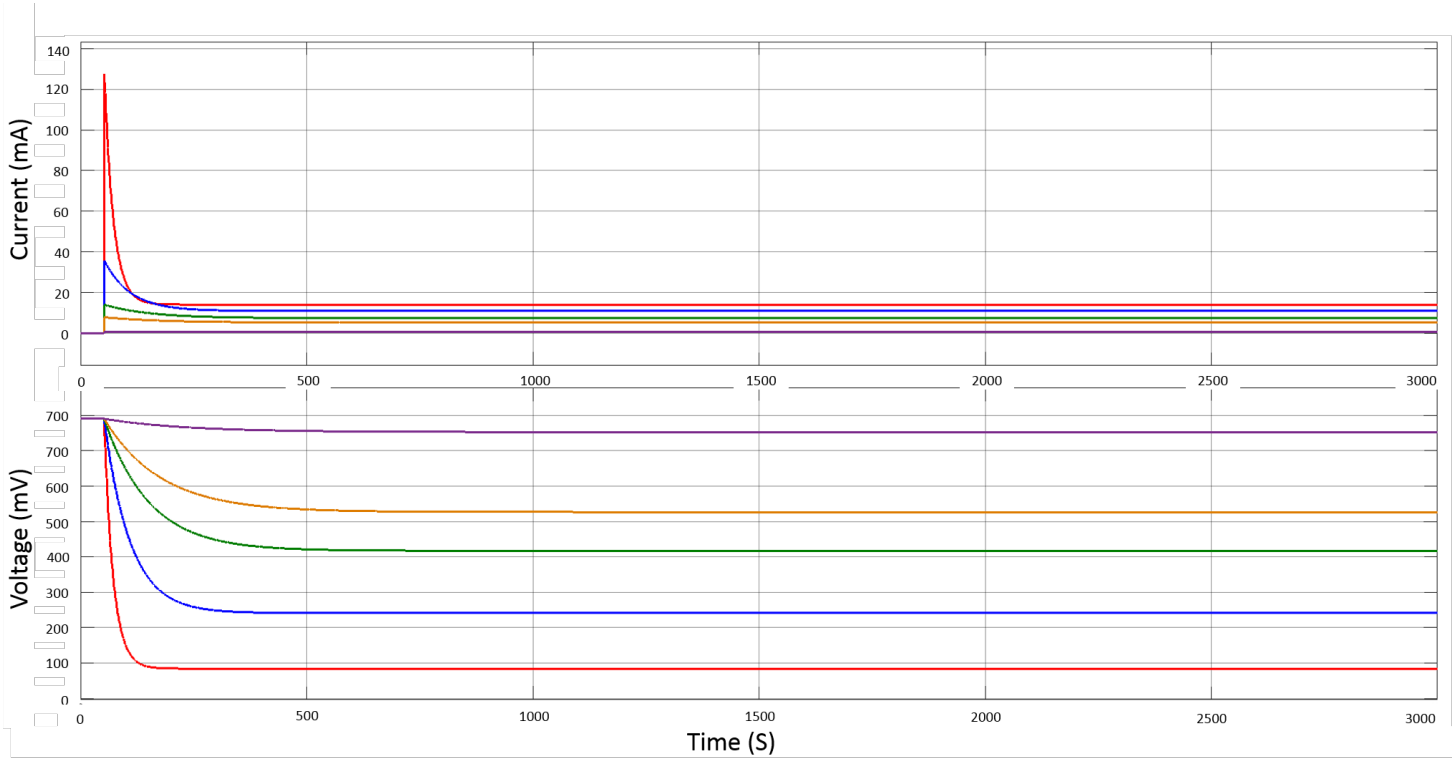

Figure 6.2: Voltage and Current Characteristics

Table 6.2: Comparison of current (mA) from field trial & simulation

Resistor(ohm)	Data from field trial	Data from simulation	Error%
6	14.75	14	5.08
22	11.25	11.5	-2.2
56	7	7.5	-7.14
100	5	5.5	-10
1000	1	1.1	-10

Simulation results of voltage are within ±18% and current are within ±10% of the field trial data. The deviation in the result might be because of connection error or measurement error.

6.2 Operating point and energy harvesting rate

The proposed model can be used to determine the operating voltage and current for a given load. For the designed circuit in chapter 4 the load resistance from the source side is 22 ohm. So from the model, we can find the input voltage and current to the load from the developed model. Figure 6.3 shows the voltage and current characteristics for the given load. We can say from the figure that at this load the input voltage to the load will be 230mv and the current will be 11.5mA and the power will 2645 mW. Figure 6.4 & 6.5 shows the mentioned operating point on the I-V and P-V graphs respectively. From the field experiment, we measured the power to be 2531 mW where the error in measurement is just 4.49%.

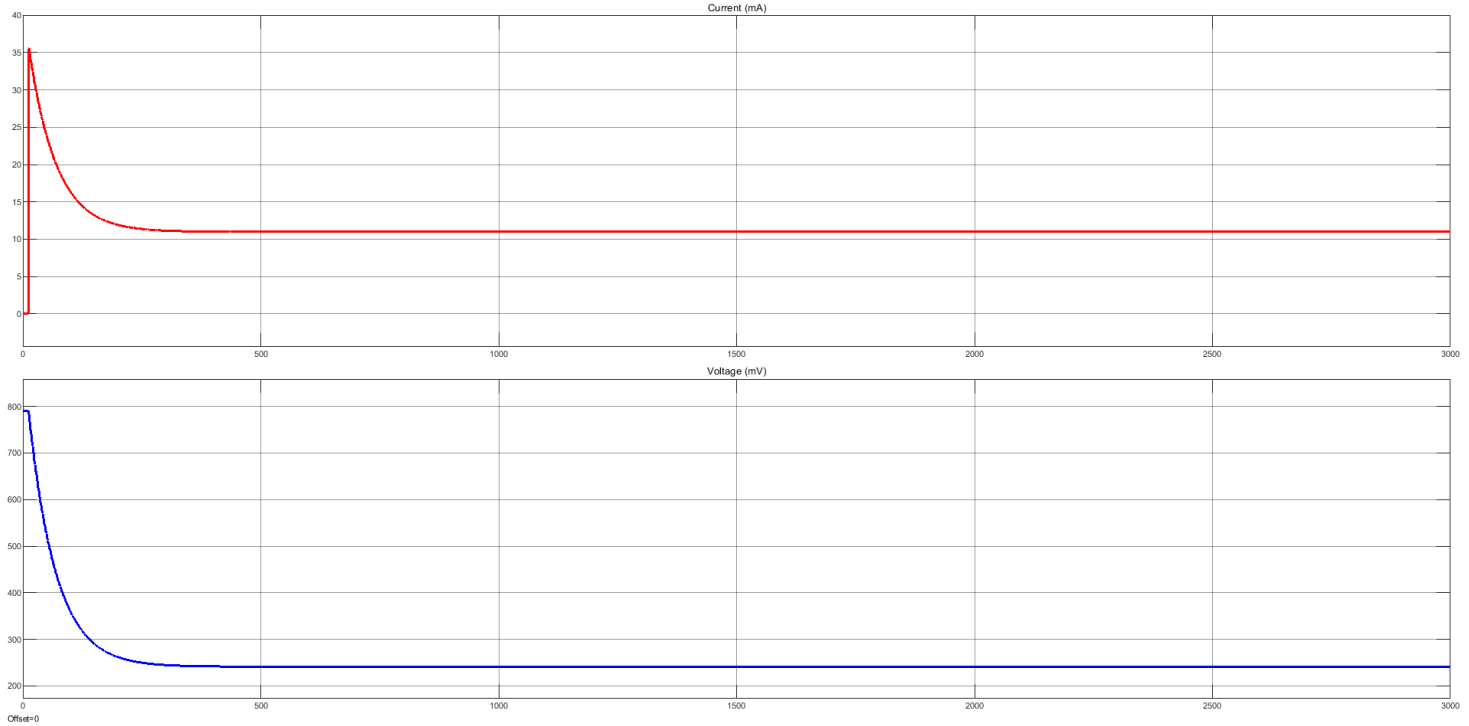

Figure 6.3: Voltage and current characteristics obtained using proposed model

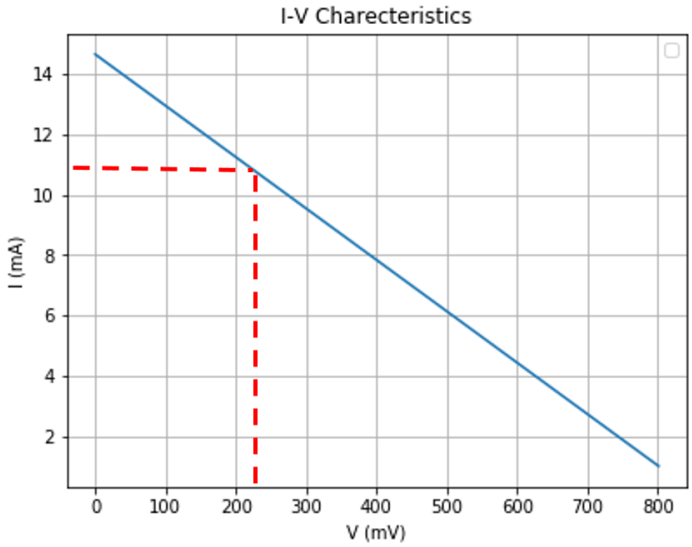

Figure 6.4: I-V Characteristics

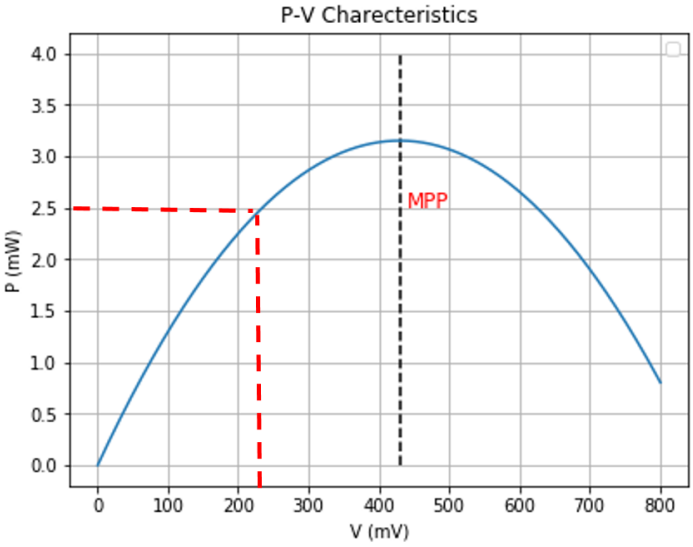

Figure 6.5: P-V Characteristics

Chapter 7

Conclusion

Identification of the corrosion status of any structure in service is very important in practical engineering. In this work, a WS node prototype is proposed and implemented for monitoring corrosion characteristics of underground water pipelines, where the node is powered by the harvested energy from the soil. Literature is replete with different energy harvesting techniques however, harvesting energy from the ground has not been explored. The preliminary results obtained from our test benches are encouraging, thus supporting more research into the design of a WSN powered with energy harvested from the soil.

The developed prototype utilizes the existing setup for the SACP to meet the energy requirements of the node. During the design and the development phase, we have explored and tested different communication modules to come up with the best solution for this particular application. WS node DC9018B-B has very low power consumption in comparison to the WiFi or the GSM module but lacks in range and scalability, whereas the MRK GSM 1400 has significantly higher power consumption but offers the range and scalability. The power consumption of the modules was analyzed to understand the feasibility of the module for this application. Our results show that the GSM module operated by the harvested energy from the soil is able to successfully report data to the cloud every day. This reporting frequency is enough for the application under consideration. The reported rate of energy harvesting is more than enough to fulfill the power requirements of the sensor node, compared to the current practice where measurements are reported manually every month.

To develop the module and perform experiments, two test benches were prepared. One is set up inside the lab under a controlled environment, whereas, the other one is set up outside, to observe the behavior of the energy source under varying weather conditions.

Several tests were carried out on both the test benches to characterize the energy source and develop a model. An equivalent circuit model has been presented in this literature which was later used to model the overall system. This model is used to find the charging characteristics of a super-capacitor.

The harvested energy from the soil is in the order of a few milliwatts which imposes a tremendous challenge in circuit design and implementation. Due to the low energy harvesting rate, it is only applicable to applications where reporting frequencies are less. There are thousands of applications in environment monitoring, structural monitoring sector where monitoring is essential but has very limited powering options. Moreover, for some applications, traditional powering options are not feasible at all. For such applications, harvesting energy from soil could be a promising solution.

In the future, the work can be extended by including the scheduler design for the optimal operation of the sensor nodes. A hierarchical network can also be considered, where sensor nodes are organized into clusters, clusters into clusters, & so on and all the sensor nodes are powered by harvested energy from the soil. This will be particularly interesting as cluster heads will tend to die more often than the edge nodes. The development of proper scheduling algorithms and knowledge of the energy status of each node will be necessary. This will also require setting up a large number of base stations to cover a given area.[11]

References

[1] André Allavena and Daniel Mossé. Scheduling of frame-based embedded systems with rechargeable batteries. In *Workshop on Power Management for Real-time and Embedded systems (in conjunction with RTAS 2001)*, 2001.

[2] Arduino. Arduino mkr gsm 1400, 2019.

[3] Arduino. Getting started with the mkr wifi 1010, 2019.

[4] V Ashworth. 4.18. principles of cathodic protection. *Shreir's Corros; Elsevier: New York, NY, USA*, pages 2747–2762, 2010.

[5] IEEE Standards Association et al. 802.15. 4-2011 ieee standard for local and metropolitan area networks-part 15.4: Low-rate wireless personal area networks (lr-wpans). *IEEE Standards Association*, 2011.

[6] Naing Naing Aung, Edward Crowe, and Xingbo Liu. Development of self-powered wireless high temperature electrochemical sensor for in situ corrosion monitoring of coal-fired power plant. *ISA transactions*, 55:188–194, 2015.

[7] MESSAOUDA Azzouzi and MILAN Stork. Modelling and simulation of a photovoltaic cell considering single-diode model. *Recent Advances in Environmental Science and Biomedicine*, pages 175–182, 2014.

[8] Stephen SO Burgess, Mark L Kranz, Neil E Turner, Rachel Cardell-Oliver, and Todd E Dawson. Harnessing wireless sensor technologies to advance forest ecology and agricultural research. *Agricultural and Forest Meteorology*, 150(1):30–37, 2010.

[9] Aimee Byrne, Niall Holmes, and Brian Norton. State-of-the-art review of cathodic protection for reinforced concrete structures. *Magazine of Concrete Research*, 68(13):664–677, 2016.

[10] IEEE Computer Society LAN MAN Standards Committee. Wireless lan medium access control (mac) and physical layer (phy) specifications. *ANSI/IEEE Std. 802.11-1999*, 1999.

[11] Hong-Ning Dai, Hao Wang, Guangquan Xu, Jiafu Wan, and Muhammad Imran. Big data analytics for manufacturing internet of things: opportunities, challenges and enabling technologies. *Enterprise Information Systems*, pages 1–25, 2019.

[12] Analog Devices. Energy harvesting multi-source demo board, May 2019.

[13] Analog Devices. Smartmesh ip rf certified eval/dev mote, May 2019.

[14] Analog Devices. Smartmesh ip rf certified eval/dev mote (mmcx antenna connector with 2dbi dipole antenna), May 2019.

[15] Analog Devices. Smartmesh ip wireless 802.15.4e pcba module with antenna connector, May 2019.

[16] Analog Devices. Ultralow voltage step-up converter and power manager, May 2019.

[17] Lance Doherty, William Lindsay, and Jonathan Simon. Channel-specific wireless sensor network path data. In *2007 16th International Conference on Computer Communications and Networks*, pages 89–94. IEEE, 2007.

[18] Bogdan Dziadak, Łukasz Makowski, and Andrzej Michalski. Survey of energy harvesting systems for wireless sensor networks in environmental monitoring. *Metrology and Measurement Systems*, 23(4):495–512, 2016.

[19] Claudio Legena Farid Touati, Alessio Galli, Damiano Crescini, Paolo Crescini, and Adel Ben Mnaouer. Environmentally powered multiparametric wireless sensor node for air quality diagnostic. *Sensors and Materials*, 27(2):177–189, 2015.

[20] P E FRANCIS. Cathodic protection, 2019.

[21] Alvaro García and Manfred N Partl. How to transform an asphalt concrete pavement into a solar turbine. *Applied Energy*, 119:431–437, 2014.

[22] N Goodman, T Muster, P Davis, S Gould, and D Marney. Accelerated test based on eis to predict buried steel pipe corrosion. *Corrosion & Prevention*, 2013.

[23] Denny A Jones. *Principles and prevention of corrosion*. Macmillan, 1992.

[24] Aman Kansal, Jason Hsu, Sadaf Zahedi, and Mani B Srivastava. Power management in energy harvesting sensor networks. *ACM Transactions on Embedded Computing Systems (TECS)*, 6(4):32–es, 2007.

[25] Chris Knight, Joshua Davidson, and Sam Behrens. Energy options for wireless sensor nodes. *Sensors*, 8(12):8037–8066, 2008.

[26] Chris Knight, Joshua Davidson, and Sam Behrens. Energy options for wireless sensor nodes. *Sensors*, 8(12):8037–8066, 2008.

[27] Selahattin Kosunalp. Mac protocols for energy harvesting wireless sensor networks: Survey. *ETRI journal*, 37(4):804–812, 2015.

[28] Jie Lian, Kshirasagar Naik, and Gordon B Agnew. Data capacity improvement of wireless sensor networks using non-uniform sensor distribution. *International Journal of Distributed Sensor Networks*, 2(2):121–145, 2006.

[29] F Robert, A Rick, W Patrick, et al. 802.15. 4e-2012: Ieee standard for local and metropolitan area networks—part 15.4: Low-rate wireless personal area networks (lr-wpans) amendment 1, 2012.

[30] David Rodenas Herráiz, Kenichi Soga, Paul RA Fidler, and Nicholas de Battista. *Wireless sensor networks for civil infrastructure monitoring: a best practice guide*. Ice Publishing, 2016.

[31] Shad Roundy, Dan Steingart, Luc Frechette, Paul Wright, and Jan Rabaey. Power sources for wireless sensor networks. In *European workshop on wireless sensor networks*, pages 1–17. Springer, 2004.

[32] Dan Su, Ye Xia, and Robert Yuan. Self-powered wireless sensor network for automated corrosion prediction of steel reinforcement. *Journal of Sensors*, 2018, 2018.

[33] Guodong Sun, Guofu Qiao, and Bin Xu. Corrosion monitoring sensor networks with energy harvesting. *IEEE Sensors Journal*, 11(6):1476–1477, 2010.

[34] Yonghong Tan and Xiangdong Yin. A dynamic scheduling algorithm for energy harvesting embedded systems. *EURASIP Journal on Wireless Communications and Networking*, 2016(1):114, 2016.

[35] Tahsin Tezdogan and Yigit Kemal Demirel. An overview of marine corrosion protection with a focus on cathodic protection and coatings. *Brodogradnja: Teorija i praksa brodogradnje i pomorske tehnike*, 65(2):49–59, 2014.

[36] ZG Wan, YK Tan, and C Yuen. Review on energy harvesting and energy management for sustainable wireless sensor networks. In *2011 IEEE 13th international conference on communication technology*, pages 362–367. IEEE, 2011.

[37] W Wang, C Li, D Robert, A Zhou, and M Wasim. Full scale corrosion test on buried cast iron pipes. In *SCMT4*, pages 1681–1690. CreateSpace, 2016.

[38] Cillian Ward, Sreejith Nanukuttan, and John McRobert. The performance of a cathodic protection system in reinforced concrete structure: monitoring and service life modelling. *Proceedings of Civil Engineering Research in Ireland (CERI), Belfast, Northern Ireland*, 2014.

[39] Thomas Watteyne, Lance Doherty, Jonathan Simon, and Kris Pister. Technical overview of smartmesh ip. In *2013 Seventh International Conference on Innovative Mobile and Internet Services in Ubiquitous Computing*, pages 547–551. IEEE, 2013.

[40] Alex S Weddell, Michele Magno, Geoff V Merrett, Davide Brunelli, Bashir M Al-Hashimi, and Luca Benini. A survey of multi-source energy harvesting systems. In *2013 Design, Automation & Test in Europe Conference & Exhibition (DATE)*, pages 905–908. IEEE, 2013.

[41] Wikipedia. Ohm's law, 2019.

[42] Xuan Wu and Dong-Weon Lee. An electromagnetic energy harvesting device based on high efficiency windmill structure for wireless forest fire monitoring application. *Sensors and Actuators A: Physical*, 219:73–79, 2014.

[43] Guoliang Ye and Kenichi Soga. Energy harvesting from water distribution systems. *Journal of Energy Engineering*, 138(1):7–17, 2011.

[44] Gao Yi, Sun Guiling, Li Weixiang, and Pan Yong. Wireless sensor node design based on solar energy supply. In *2009 2nd International Conference on Power Electronics and Intelligent Transportation System (PEITS)*, volume 3, pages 203–207. IEEE, 2009.

[45] Yan Yu, Guofu Qiao, and Jinping Ou. Self-powered wireless corrosion monitoring sensors and networks. *IEEE Sensors Journal*, 10(12):1901–1902, 2010.